Age-related microbiome metabolites alter RNA splicing and chromatin accessibility in the brain

Meenakshi Chakraborty[1], Sophia M. Shi[2,3,4,5], Imani E. Porter[1], Daniel J. Richard[1], Georgi K. Marinov[1], Ashley A. Moore[6], Jenna L. E. Blum[7], Aravind Natarajan[6], James W. Jahng[8,9], Joseph C. Wu[8,9], Sydney X. Lu[6], Shawn M. Davidson[7], William J. Greenleaf[1], Nay L. Saw[10], Mehrdad Shamloo[10,11], Anne Brunet[1,5,12,13], Tony Wyss-Coray[4,5,13], Ami S. Bhatt[1,6,13,*]

[1]Department of Genetics, Stanford University, Stanford, CA, USA. [2]Department of Chemistry, Stanford University, Stanford, CA, USA. [3]Stanford Chemistry, Engineering and Medicine for Human Health (ChEM-H), Stanford University, Stanford, CA, USA. [4]Department of Neurology and Neurological Sciences, Stanford University School of Medicine, Stanford, CA, USA. [5]Wu Tsai Neurosciences Institute, Stanford University School of Medicine, Stanford, CA, USA. [6]Department of Medicine, Divisions of Hematology and Blood & Marrow Transplantation, Stanford University, Stanford, CA, USA. [7]Division of Pulmonary and Critical Care Medicine, Department of Medicine, The Feinberg School of Medicine, Northwestern University, Chicago, IL, USA. [8]Stanford Cardiovascular Institute, Stanford University School of Medicine, Stanford, CA, USA. [9]Department of Medicine, Division of Cardiovascular Medicine, Stanford University School of Medicine, Stanford, CA, USA. [10]Stanford Behavioral and Functional Neuroscience Laboratory, Wu Tsai Neurosciences Institute, Stanford University, Stanford, CA, USA. [11]Department of Neurosurgery, School of Medicine, Stanford University, Stanford, CA, USA. [12]Glenn Center for the Biology of Aging, Stanford University, Stanford, CA, USA. [13]The Phil and Penny Knight Initiative for Brain Resilience, Stanford University, Stanford, CA, USA.

*Correspondence should be addressed to Ami S. Bhatt (asbhatt@stanford.edu).

Abstract

The gut microbiome generates diverse metabolites that can enter the bloodstream and alter host biology, including brain function. Hundreds of physiologically relevant, gut-brain signaling molecules likely exist; however, there has been no systematic, high-throughput effort to identify and validate them. Here, we integrate computational, *in vitro*, and *in vivo* approaches to pinpoint microbiome-derived metabolites whose blood levels change during aging, and that induce corresponding changes in the mouse brain. First, we mine large-scale metabolomics datasets from human cohorts (each $n \geq 1200$) to identify 30 microbiome-associated metabolites whose blood levels change with age. We then screen this panel in an *in vitro* transcriptomic assay to identify metabolites that perturb genes linked to age-related neurodegeneration. We then test four metabolites in an acute-exposure mouse model, and use multi-omic approaches to evaluate their impact on cellular functions in the brain. We confirm the known neurodegeneration-promoting effects of trimethylamine N-oxide (TMAO), including mitochondrial dysfunction, and further discover its disruptive impact on the pathways of glycolysis, GABAergic signaling, and RNA splicing. Additionally, we identify glycodeoxycholic acid (GDCA), a microbiome-derived secondary bile acid, as a potent regulator of chromatin accessibility and suppressor of genes that protect the brain from age-related, neurodegeneration-promoting insults. GDCA also acutely reduces mobility. In summary, we present a scalable framework for linking microbiome metabolites to host pathologies, and apply it to identify microbial metabolites that induce molecular changes related to neurodegeneration.

Introduction

Aging is the greatest risk factor for many neurodegenerative diseases. Remarkably, age-related conditions that often precede these diseases, such as mild cognitive impairment (MCI), can be reversible[1,2]. Thus, identifying potentially modifiable age-related factors that promote neurodegeneration could alter and perhaps improve the natural history of disease initiation and progression.

One physiological compartment that changes with aging is the gut microbiome[3–5], likely due to factors such as increased permeability of the gut lining, increased medication usage, immunosenescence, and accumulated exposure to environmental toxins. In light of growing interest in the microbiota-gut-brain axis[6,7], a natural question arises: does “microbiome aging” contribute to “brain aging” and associated pathologies? Fecal microbiota transfers between young and aged mice - which can induce or reverse neuroinflammation and cognitive decline - suggest that it does[8–10]. However, the microbiome-related molecules and underlying molecular mechanisms that drive these phenotypes remain largely uncharacterized in both animals and humans, which limits translation of this knowledge to the clinic. This gap in the gut-brain field is partly due to the underutilization of *in vitro* systems, which can help create a pipeline from hypothesis-generating data analyses to *in vivo* validation.

The microbiome is known to substantially impact the levels of blood metabolites, with hundreds of metabolites differing in abundance between germ-free mice and their conventionally raised counterparts[11,12]. This is significant because blood metabolites enable the proper functioning of host organs; when their levels change, this can have profound effects on physiology[13–15]. We therefore hypothesized that microbiome aging affects brain aging by altering the levels of bioactive blood metabolites. These metabolites could impact the blood-brain barrier - a key regulator of brain homeostasis whose functionality declines with age[16] - and perhaps even cross it to act directly on neurons and glia.

To evaluate this hypothesis, we first leveraged public datasets[12,17–23] to identify a panel of 30 blood metabolites whose levels: 1) change with human aging, and 2) are significantly associated with the presence and/or composition of the gut microbiome. We then screened these candidates *in vitro* for their ability to alter the expression of genes in pathways related to age-related neurodegeneration, and validated four of the most interesting metabolites *in vivo* through multi-omic analyses of the mouse brain. Our results confirm and expand the neurodegeneration-promoting effects of the microbiome-derived metabolite trimethylamine N-oxide (TMAO), including novel effects on RNA splicing. In addition, we find that glycodeoxycholic acid (GDCA), a microbiome-derived bile acid, alters chromatin accessibility and silences many genes that maintain brain homeostasis after stress and injury. Finally, in behavioral experiments, we find that GDCA, whose blood levels are correlated with neurodegeneration and cognitive impairment in multiple human cohorts[24–28], acutely reduces mobility. Together, our findings on TMAO and GDCA, our curated panel of age- and microbiome-associated blood metabolites, and the integrative framework we present - combining computational, *in vitro*, and *in vivo* approaches - provide a foundation for substantial advances in identifying microbiome-derived molecules that play key roles in host physiology.

Results

Identifying microbiome-associated metabolites whose blood levels change with age

There have been extensive efforts to characterize the specific metabolomic changes that occur with aging[17]. In addition, recent work has identified metabolites associated with microbiome composition and activity[11,12,21–23]. We leveraged these data to build a panel of metabolites for medium-throughput *in vitro* testing (Fig. 1; Supplementary Table 1; Methods).

Specifically, we first referenced a recent review on the metabolomics of aging[17] to identify three large cohort studies[18–20] that each analyzed blood samples from at least 1,200 participants. Pooling data across these studies yielded hundreds of metabolites whose blood levels changed with age in at least one study. Separately, we curated a list of human-associated metabolites that have been reported to be produced by microbes, either alone or via host-microbe "cometabolism" (where both host and microbial metabolism contribute to the final product). Intersecting this curated list with the age-associated metabolites yielded 79 unique overlapping metabolites.

For experimental feasibility, we further narrowed the list, prioritizing metabolites most strongly linked to the gut microbiome. We used two key resources: **(1)** a recent study comparing blood metabolite levels between germ-free and conventionally raised mice[12]; and **(2)** the GUTSY Atlas[22], which reported the proportion of variance in blood metabolite levels "explained" by the gut microbiome for 1,168 metabolites based on paired stool-blood data for over 8,000 humans. Metabolites were retained for the final panel if they met at least one of two criteria: **(1)** showed significantly different blood levels between germ-free and conventionally raised mice[12]; **(2)** ranked in the top 20% of blood metabolites for the GUTSY variance-explained metric.

We eliminated alanine because it is expected to have minimal impact on cellular processes[29], and uridine because its blood levels increased with age in one study[18] but decreased with age in another[20]. The final panel comprised 30 metabolites, 26 of which increased with age and 4 of which decreased with age (Supplementary Table 1). The metabolites encompassed a broad spectrum of categories, spanning six super classes, thirteen classes, and sixteen sub classes within the Human Metabolome Database (HMDB)[30] taxonomy (Fig. S1).

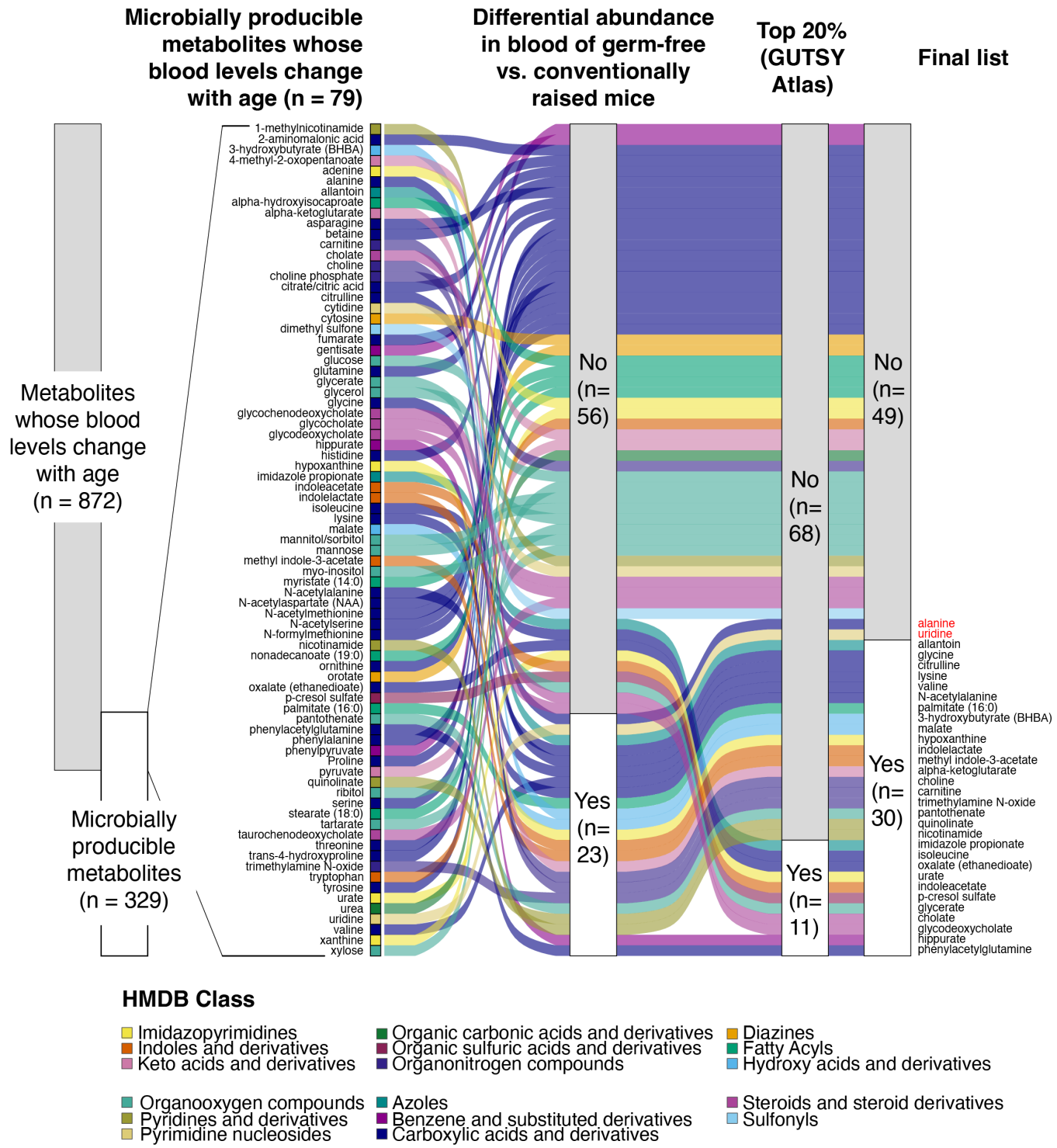

Fig. 1. Workflow used to define a panel of 30 microbiome-associated metabolites whose blood levels change with age. First, metabolites whose blood levels changed with age in large cohort(s) were overlapped with a curated list of metabolites that are producible by microbes, either alone or via host-microbe cometabolism. Metabolites were retained for the final panel if they met at least one of two criteria: **(1)** showed significantly different blood levels in germ-free vs. conventionally raised mice (based on Lai *et al.*, 2021[12]), and/or **(2)** ranked in the top 20% for the proportion of

variance in blood levels "explained" by the gut microbiome (metric from the GUTSY Atlas[22]). After excluding alanine and uridine (see Results), the final panel comprised 30 metabolites.

In vitro screening reveals that microbiome-associated metabolites perturb genes and pathways linked to age-related neurodegeneration

While *in vivo* validation remains the gold standard for assessing physiological relevance, we began with *in vitro* screening, as testing dozens of metabolites *in vivo* for potential effects on the brain would not have been practically feasible. We chose human brain endothelial cells as our model system because they line the brain's blood vessels and are the first brain cell type encountered by blood metabolites. In fact, many blood metabolites never reach other brain cell types, since endothelial cells are a key component of the blood-brain barrier (BBB), which selectively regulates entry into the brain parenchyma. Importantly, even metabolites that do not cross the BBB could significantly impact brain function, since BBB decline is a defining feature of brain aging and neurodegeneration[16].

We chose to use hCMEC/D3 cells, an immortalized human brain endothelial cell line widely used in BBB studies[31]. To conduct the screen, each metabolite was added individually to low-passage hCMEC/D3 cells in triplicate, alongside matched vehicle controls containing the corresponding solvent in the media (Fig. 2A; Supplementary Table 3). After a 3-hour incubation (chosen over longer timepoints to minimize metabolite clearance), cells were lysed in TRIzol for downstream RNA extraction and sequencing. Each metabolite was added at a representative physiological concentration, primarily based on its listed blood concentrations in HMDB (Methods; Supplementary Table 1). In addition to vehicle controls, we included lipopolysaccharide (LPS) controls in each sequencing batch, given the known effects of LPS on human brain endothelial cells[32]. As expected, LPS induced the expression of genes in KEGG pathways associated with inflammation, such as "TNF signaling pathway" and "NOD-like receptor signaling pathway" (Fig. 2B; Fig. S2; Supplementary Table 2).

The number of differentially expressed genes (DEGs), relative to vehicle controls, varied considerably across the 30 test metabolites, reflecting substantial differences in the magnitude of their transcriptional impact (Fig. S3; Supplementary Tables 4-5). The median number of DEGs was 45.5, with an interquartile range (IQR) of 18.5 to 359.5, and a total range of 3 to 6,419 genes affected. Twelve metabolites perturbed ≥5 genes in the KEGG pathways for "Alzheimer's Disease" (AD) and/or "Parkinson's Disease" (PD), which are the two most common age-related neurodegenerative disorders (Fig. 2C; Supplementary Table 6). The affected AD/PD genes converged on processes including energy metabolism, proteasome-mediated protein degradation, and inflammatory signaling, whose disruptions are central to neurodegenerative disease[33].

We prioritized four metabolites for *in vivo* validation of their effects on brain function: indoleacetic acid (IAA), glycodeoxycholic acid (GDCA), trimethylamine N-oxide (TMAO), and palmitic acid (PA). TMAO's effects on the brain have been studied previously[34], so we included it partially as a control and also to expand the scope of knowledge about its impact on the brain. All four chosen metabolites share the following characteristics (Fig. 2D). They **(1)** impact the expression of at least 5 unique genes in the AD and/or PD KEGG pathways in our transcriptomic screen (Fig. 2C), **(2)** increase in the blood with age (Supplementary Table 1), **(3)** have been

associated with AD, PD, and/or impaired cognition in humans[24–28,34–39], **(4)** are strongly associated with production or regulation by the gut microbiome[12,22,40,41], and **(5)** have been detected in human cerebrospinal fluid and/or brain[42–46].

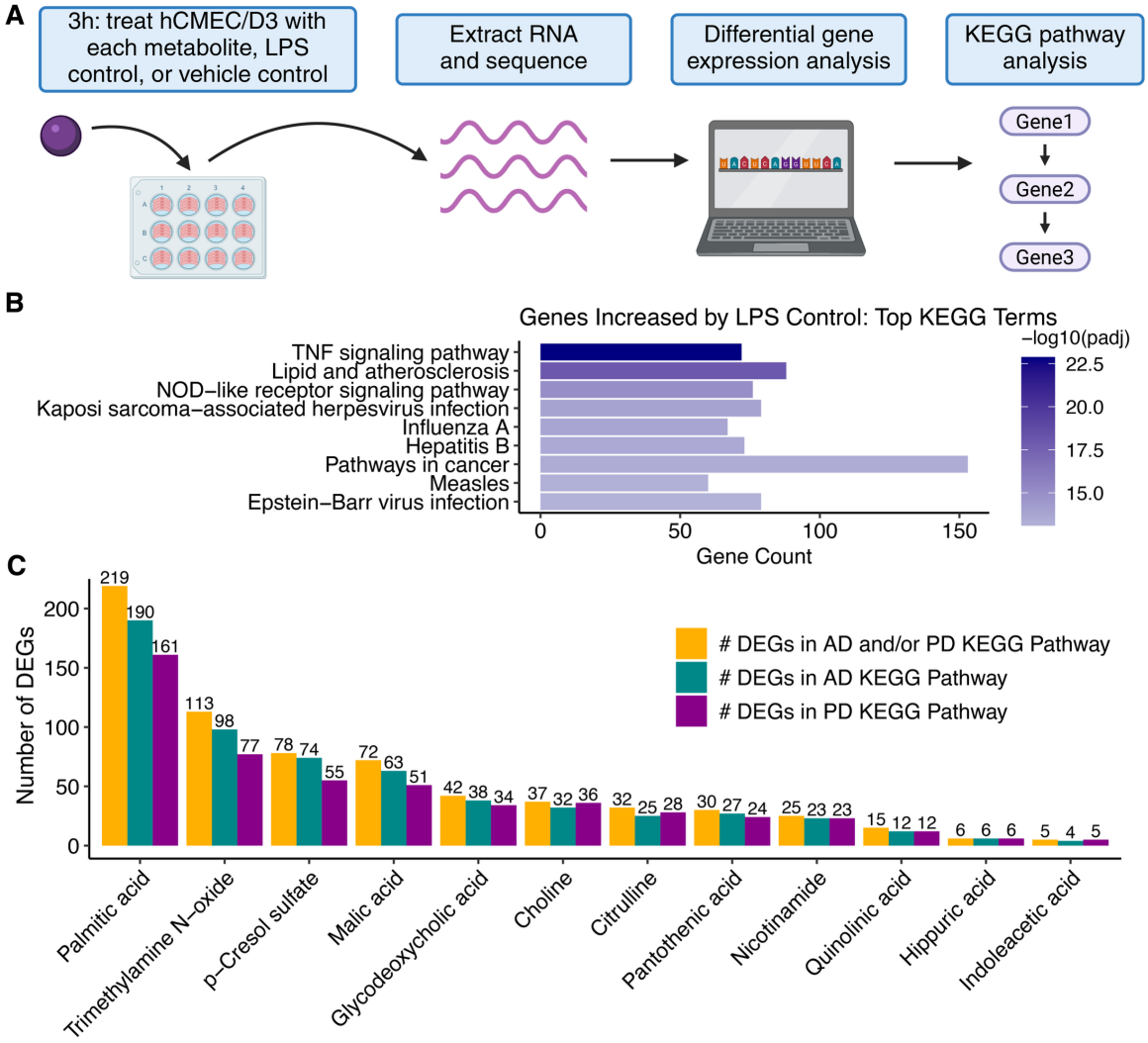

Criteria	IAA	GDCA	TMAO	PA
Unique AD/PD genes	5	42	113	219
Up with age?	Y	Y	Y	Y
Associated with AD, PD, or impaired cognition?	Y	Y	Y	Y
Strong association with gut microbiome?	Y: 92nd percentile GUTSY	Y: 91st percentile GUTSY	Y: near-absent in GF mice	Y: ~2x higher in GF mice
In CSF or brain?	Y	Y	Y	Y

Fig. 2. *In vitro* screening reveals that microbiome-associated metabolites perturb genes and pathways linked to age-associated neurodegenerative disease. **(A)** Schematic illustrating the

173 setup of the *in vitro* transcriptomic screen. The full panel of 30 metabolites was distributed across
174 four sequencing batches, with each metabolite included in one batch. Within each batch, at least
175 *n*=3 wells were treated with each assigned metabolite, its respective vehicle control, or the LPS
176 control (see Methods and Supplementary Table 3). **(B)** Top enriched KEGG pathways for the
177 genes significantly upregulated by the LPS control in the first sequencing batch. The analogous
178 results for batches #2-4 are presented in Fig. S2. The non-specific "KEGG root term" was filtered
179 out. **(C)** Number of differentially expressed genes (DEGs) per metabolite in the KEGG pathways
180 for Alzheimer's Disease (AD) and Parkinson's Disease (PD). Metabolites impacting at least 5
181 unique AD/PD genes are shown. **(D)** Identity and characteristics of the four metabolites chosen
182 for subsequent *in vivo* validation of their effects on the brain. IAA = indoleacetic acid, GDCA =
183 glycodeoxycholic acid, TMAO = trimethylamine N-oxide, PA = palmitic acid, AD = Alzheimer's
184 Disease, PD = Parkinson's Disease, GF = germ-free, CSF = cerebrospinal fluid. GUTSY refers to
185 the GUTSY Atlas[22], which reports microbiome-attributable variance in blood levels for 1,168 blood
186 metabolites. Structure diagrams were produced with rdkit[47]. Relevant studies (e.g., those
187 reporting metabolite detection in CSF or brain) are cited in the text.

188 TMAO disrupts transcriptional homeostasis and RNA splicing in the mouse 189 brain

190 To interrogate the effects of each of the four chosen metabolites on cellular functions in the brain
191 *in vivo*, we conducted bulk transcriptomics on mouse brain hemispheres following intravenous
192 retro-orbital injection of each metabolite or vehicle (2-hour treatment; *n*=4 male mice per injection
193 group; Fig. 3A). Doses were chosen to reflect physiologically relevant exposures, by converting
194 blood concentrations previously observed in seniors[26,28,48–55] to mouse-equivalent doses using
195 well-established scaling guidelines[56,57]. This experiment design was informed by prior work on
196 TMAO[58], such that TMAO could serve as a positive control. The main modification was the use
197 of intravenous retro-orbital injection - a well-established technique[16,59–61] - in place of
198 intraperitoneal injection, to enable direct entry into systemic circulation and more precise control
199 of blood metabolite levels.

200 For TMAO, the chosen mouse dose was 1.8 mg/kg, the same as the original study[58],
201 approximating 30μM concentration in human blood. The remaining doses were 22.2 mg/kg for PA
202 (~100μM human), 1.5 mg/kg for IAA (~10μM human), and 0.4 mg/kg for GDCA (~1μM human).
203 All human-equivalent concentrations were non-cytotoxic *in vitro* in hCMEC/D3 cells (Fig. S7). For
204 PA - unlike for the other metabolites - the human-equivalent concentration used for the mouse
205 experiment was reduced relative to the concentration used in the *in vitro* transcriptomic screen.
206 This was because the original concentration of 500μM was cytotoxic to hCMEC/D3 cells (Fig. S7),
207 likely explaining the disproportionately large number of DEGs observed for PA *in vitro* (Fig. S3).
208 Overall, the cytotoxicity testing (Fig. S7) ensured that the mouse exposures reflected
209 physiologically relevant human levels while avoiding human concentrations that are overtly
210 cytotoxic.

211 PA and IAA had negligible effects on gene expression in the mouse brain, with fewer than
212 ten differentially expressed genes per metabolite (Fig. 3B; Supplementary Table 7). By contrast,
213 TMAO and GDCA each had a significant transcriptional impact in the brain, modulating the
214 expression of 2,305 and 179 genes, respectively (Fig. 3C; Supplementary Table 7). We first

evaluated the TMAO results to verify concordance with the literature and also to derive additional insights about the impact of this microbiome metabolite on brain function.

In agreement with prior literature[58], we observed a coordinated downregulation of mitochondrially-encoded genes involved in oxidative phosphorylation, including *mt-Nd1, mt-Nd2, mt-Nd3, mt-Co2, mt-Co3, mt-Cytb, mt-Atp6,* and *mt-Atp8* (Supplementary Table 7). However, gene set enrichment analysis (GSEA) based on hallmark gene sets revealed a more complex rewiring of bioenergetic pathways (Fig. 4A; Supplementary Table 8). Despite the clear downregulation of mitochondrial oxidative phosphorylation, the term “oxidative phosphorylation” was positively enriched in GSEA when comparing TMAO-treated brains to controls. This result was due to the upregulation of several nuclear-encoded genes involved in oxidative phosphorylation (e.g., *Cox4i1, Cox6a1, Cox6b1, Cox7a2l, Ndufa7, Ndufa8, Ndufb2, Ndufb6, Ndufb8, Ndufc2*), perhaps reflecting a compensatory response, similar to that observed in patients with macro-deletion of mtDNA[62].

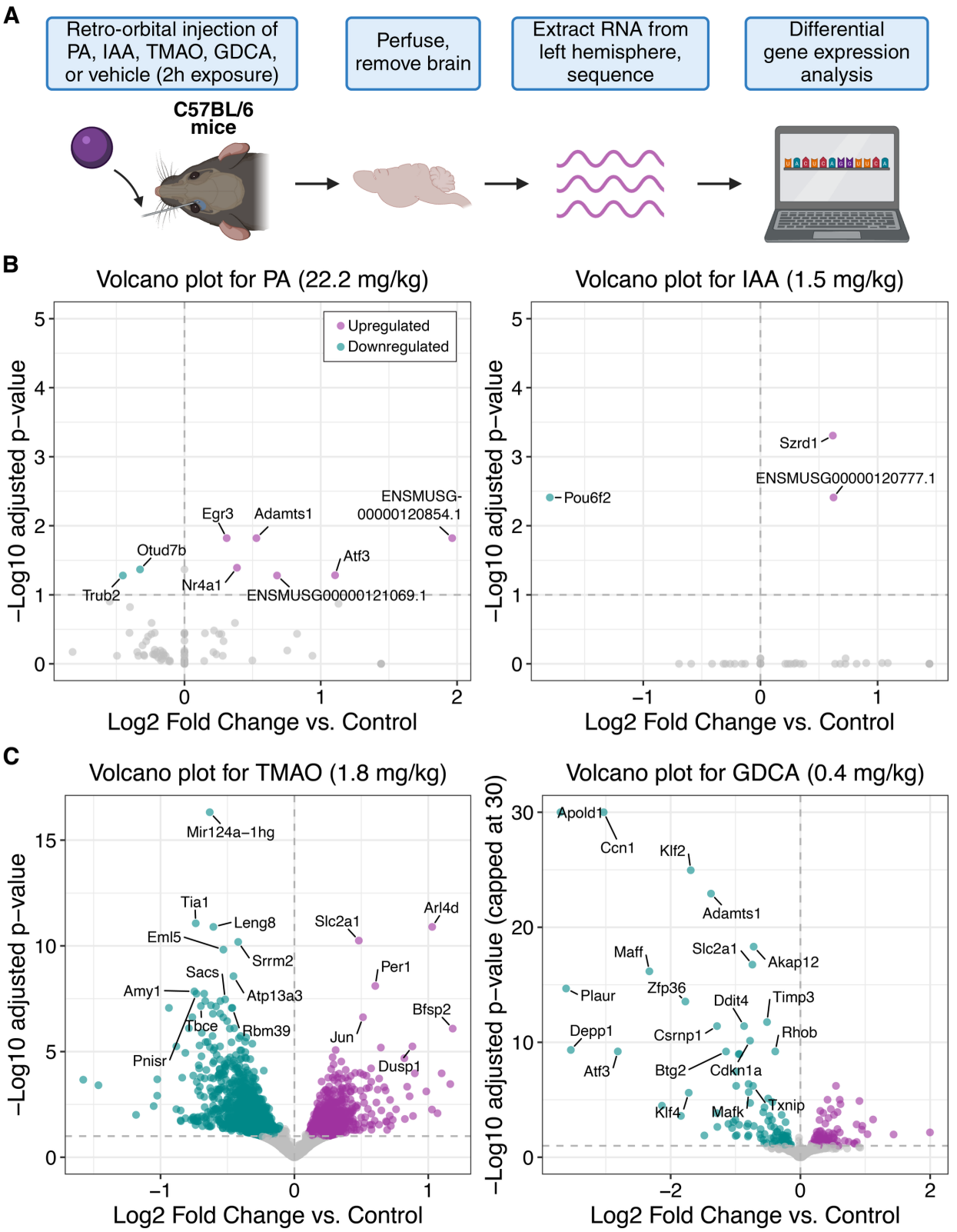

Fig. 3. The four metabolites selected for *in vivo* experiments impact brain gene expression to markedly different extents. **(A)** Schematic illustrating the setup of the *in vivo* transcriptomics experiment; *n*=4 C57BL/6 male mice were injected with each metabolite or vehicle. **(B)** Volcano

233 plots showing the results of differential gene expression analysis between PA- and IAA-treated
234 brains and their vehicle controls. **(C)** Volcano plots showing the results of differential gene
235 expression analysis between TMAO- and GDCA-treated brains and their vehicle controls. In both
236 **(B)** and **(C)**, the y-axis represents the -log10(adjusted *p*-value) from DESeq2, and the x-axis
237 represents the log2FoldChange vs. vehicle control, after applying the recommended
238 log2FoldChange shrinkage via lfcShrink[63]. Purple dots represent significantly upregulated genes,
239 with an adjusted $p \leq 0.1$ (DESeq2 default) and shrunken log2FoldChange ≥ 0.1. Teal dots
240 represent significantly downregulated genes (adjusted $p \leq 0.1$ and shrunken log2FoldChange ≤ -
241 0.1). The y-axis for the GDCA volcano plot was capped at 30 to avoid distortion by extreme
242 values; the non-capped, adjusted *p*-values for *Apold1* and *Ccn1* are 1.82E-108 and 3.50E-70,
243 respectively (Supplementary Table 7).
244
245 In addition, GSEA highlighted the term "glycolysis" as enriched (Fig. 4A). Indeed, eight
246 glycolytic genes were upregulated by TMAO, including *Hk1* and *Pkm*, which catalyze rate-limiting
247 steps of glycolysis[64] (Fig. 4B; Supplementary Table 7). Furthermore, *Slc2a1* (i.e., *Glut1*), a major
248 glucose transporter in the brain that supports glycolytic flux, was the second most significantly
249 upregulated gene by TMAO (adjusted *p*-value 5.62E-11; Fig. 3C and Supplementary Table 7).
250 These findings agreed with data from our *in vitro* transcriptomic screen, where TMAO upregulated
251 human glycolytic genes including *HK1*, *PKM*, *PFKP*, *GPI*, and *ALDOA* (Supplementary Table 5).
252 Overall, our results align with previous findings that TMAO results in mitochondrial dysfunction in
253 the brain[34]. Furthermore, our findings demonstrate a previously unreported upregulation of the
254 glycolytic pathway in the brain.
255 Mitochondrial dysfunction can cause oxidative stress. Consistent with this, the "reactive
256 oxygen species pathway" was significantly more highly expressed (Fig. 4A) in the brain
257 transcriptome of TMAO-exposed animals vs. controls. In addition, *Txnip* - a known inducer of
258 oxidative stress and activator of the inflammasome[65] - was significantly upregulated by TMAO
259 (Supplementary Table 7). This finding is consistent with the most enriched GSEA term, "TNFα
260 signaling via NF-κB" (Fig. 4A), which reflects inflammatory signaling. Together, these results
261 support previous studies showing that TMAO promotes oxidative stress and inflammation,
262 including in the brain[34,66,67].
263 GSEA using the REACTOME pathway database provided additional insights, including
264 the positive enrichment of genes involved in synaptic transmission and GABAergic signaling,
265 especially genes related to $GABA_B$ receptor activation (Fig. 4C; Supplementary Table 8). By
266 contrast, we observed a marked downregulation of genes encoding $GABA_A$ receptors (Fig. S8).
267 These results suggest that TMAO may shift inhibitory neural circuits from fast $GABA_A$-mediated
268 responses towards slower, $GABA_B$-mediated responses. Although previous literature has
269 demonstrated negative effects of TMAO on synaptic function[34], this is the first observation, to our
270 knowledge, of specific perturbation of GABAergic signaling pathways. To assess the extent of
271 TMAO's impact on neuronal cells vs. other brain cell types, we computed "marker genes" for six
272 different brain cell classes, using a well-characterized single-cell dataset from the mouse brain[68]
273 (Methods). TMAO downregulated over 15% of the marker genes for cells in the neuronal lineage,
274 representing more than twice its impact on any of the other five cell classes (Fig. 4D).
275 GSEA also highlighted the depletion of genes associated with "mRNA splicing" (Fig. 4C).
276 Strikingly, several of the genes that were most significantly downregulated by TMAO (e.g., *Tia1*,

Srrm2, *Pnisr*, and *Rbm39*, see Fig. 3C and Supplementary Table 7) regulate alternative splicing[69–72]. This result was intriguing given the well-established link between changes in splicing patterns and the development of neurological disease[73].

Given the observed impact of TMAO on splicing-related factors, we sought to determine whether any genes were differentially spliced in TMAO-treated animals vs. controls. In agreement with the changes in splicing factor expression, the widely used rMATS-turbo software[74] nominated 126 differential splicing events between TMAO-treated and vehicle-treated brains, which we narrowed to 44 using conservative filters (Fig. 4E; Supplementary Table 9; Methods). Manual inspection in Integrative Genomics Viewer (IGV) revealed clear patterns consistent with differential splicing, including that of *Kmt2b*, a gene whose aberrant splicing has been linked to dystonia[75,76], a movement disorder that can occur independently or as a symptom of Parkinson's disease (Fig. S9). *Kmt2b* also exhibited differential expression in TMAO- vs. vehicle-treated brains (log2FoldChange -0.39, adjusted *p* 0.001; Supplementary Table 7), potentially as a consequence of its differential splicing.

To our knowledge, this is the first demonstration of TMAO regulating alternative splicing patterns. Overall, our findings confirm[34,58] and broaden current understanding of TMAO's neurodegeneration-promoting effects, which we summarize in a unified model (Fig. 4F).

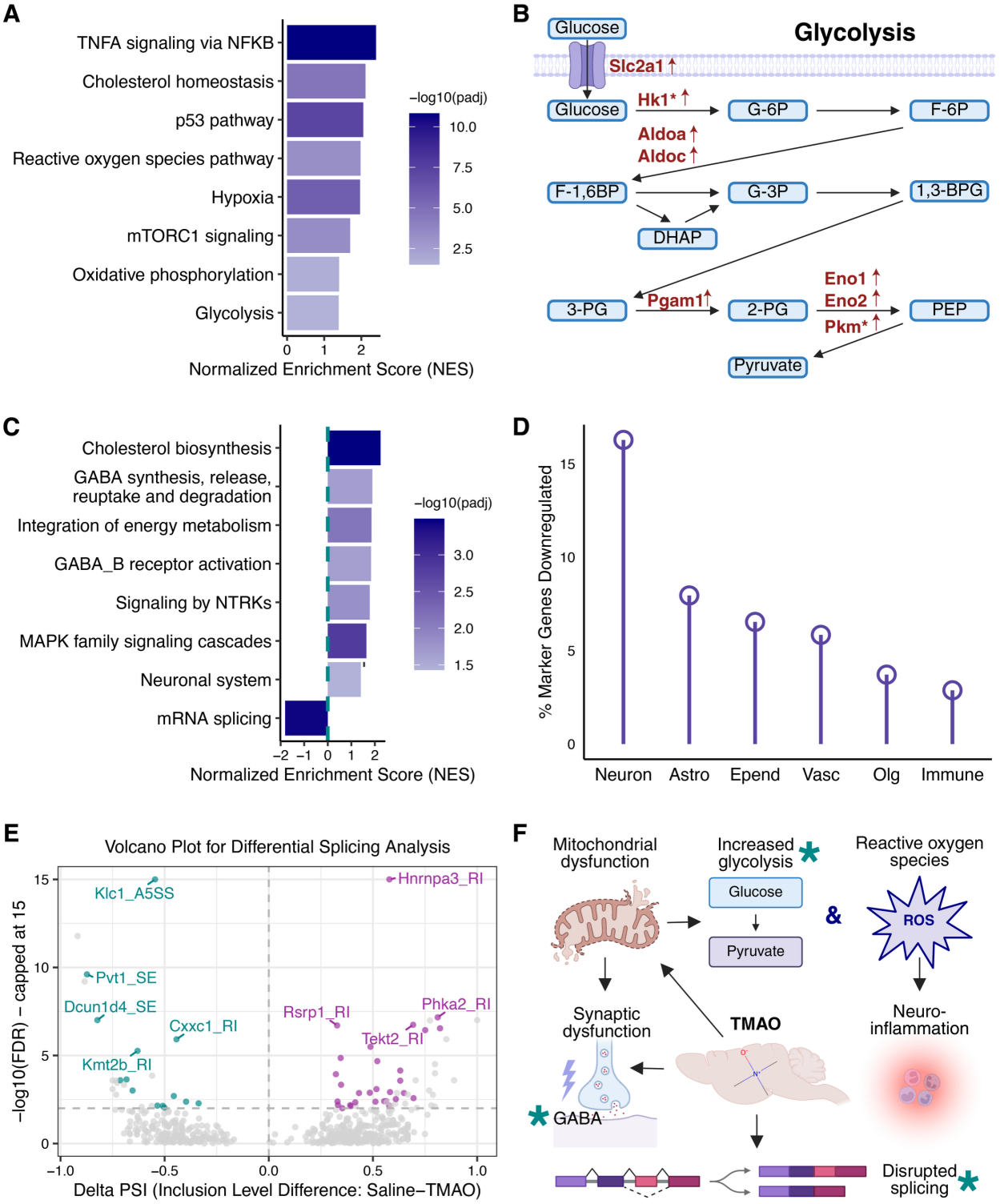

Fig. 4. TMAO disrupts transcriptional homeostasis and RNA splicing in the mouse brain. **(A)** Selected significantly enriched terms from gene set enrichment analysis (GSEA) based on hallmark gene sets; full results in Supplementary Table 8. **(B)** The glycolysis pathway, annotated with the glycolytic genes upregulated by TMAO. * = genes whose products catalyze rate-limiting

300 steps of glycolysis. Base figure adapted from Hu *et al.*, 2014[77]. **(C)** Selected significantly enriched
301 terms from GSEA using the REACTOME pathway database; full results in Supplementary Table
302 8. **(D)** Percentage of marker genes in each brain cell class that are downregulated by TMAO.
303 Neuron = neuronal lineage, Astro = astrocyte lineage and stem cells, Ependm = ependymal cells,
304 Vasc = vasculature cells, Olg = oligodendrocyte lineage, Immune = immune cells. **(E)** Results of
305 differential splicing analysis comparing brains from TMAO-exposed and control mice. Each point
306 represents a splicing event. The x-axis represents the inclusion level difference (ΔPSI) and the y-
307 axis represents the -log10(FDR), capped at 15 for visual clarity. Events significantly enriched in
308 control or TMAO are shown in purple and teal, respectively; non-significant events are shown in
309 gray. To reduce visual clutter, points were filtered to those with -log10(FDR) > 0. RI = retained
310 intron, A5SS = alternative 5' splice site, SE = skipped exon. **(F)** Unified model of TMAO's
311 neurodegeneration-promoting effects on the brain. Asterisks indicate portions of the model that
312 are novel based on insights derived from this study. TMAO induces mitochondrial dysfunction,
313 leading to compensatory upregulation of glycolysis and increased production of reactive oxygen
314 species (ROS). The resulting oxidative stress further promotes neuroinflammation. Perhaps as a
315 result of the rewired bioenergetic state, TMAO also promotes synaptic dysfunction, including
316 impairments in GABAergic transmission. In addition, it downregulates splicing factors, resulting in
317 changes to splicing patterns.

318 GDCA remodels chromatin and dramatically suppresses genes that protect 319 the brain from stress and injury

320 Like TMAO, GDCA is a well-known microbiome-derived metabolite. It is a secondary conjugated
321 bile acid, formed when the host conjugates microbially produced DCA with glycine. Blood levels
322 of GDCA have been associated with neurodegeneration and/or cognitive impairment in at least
323 five studies[24–28] (summarized in Supplementary Table 10). However, GDCA's brain-specific
324 effects have not, to our knowledge, been experimentally evaluated in mammals.
325 GDCA strongly suppressed the expression of many genes in the mouse brain (Fig. 3C;
326 Supplementary Table 7). The most significantly downregulated gene was *Apold1*
327 (log2FoldChange -3.7, adjusted *p*-value 1.82E-108), a gene whose expression is critical for stroke
328 recovery in mice[78]. *Ccn1*, the second most downregulated gene (log2FoldChange -3.0, adjusted
329 *p*-value 3.50E-70), similarly promotes wound healing and tissue repair[79]. This pattern extended
330 beyond individual genes: many of the genes that were strongly downregulated by GDCA (e.g.,
331 *Klf2*, *Klf4*, *Adamts1*, *Akap12*, *Maff*, *Plaur*, *Ddit4*, *Atf3*, *Btg2*) are involved in cellular responses to
332 injury and stress, including oxidative stress, hypoxia, DNA damage, and stroke[80–88]. These
333 observations were supported by GSEA based on hallmark gene sets. GSEA demonstrated
334 significant negative enrichment of the terms "TNFα signaling via NF-κB" and "hypoxia" (Fig. 5A),
335 as well as nominal negative enrichment of "p53 pathway" (Supplementary Table 8), consistent
336 with reduced activity of stress-response pathways. The results suggested marked disruption of
337 endothelial cell homeostasis; for example, the simultaneous reductions of *Klf2* and *Klf4* alone
338 would be expected to cause severe endothelial dysfunction[89,90]. However, given the use of bulk
339 RNA-seq, it is unknown whether these decreases originated specifically from endothelial cells, or
340 from other brain cell types.

341 GSEA using the REACTOME pathway database (Fig. 5B; Supplementary Table 8)
342 demonstrated the positive enrichment of several terms related to chromatin dynamics, including
343 "PKMTs methylate histone lysines," "epigenetic regulation of gene expression," and "chromatin
344 organization." Based on this result, we postulated that GDCA achieves its notable gene regulatory
345 effects, including the strong silencing of many genes, by inducing changes in chromatin
346 organization and accessibility. To test this hypothesis, we conducted bulk ATAC-Seq on the flash-
347 frozen right brain hemispheres of the GDCA- and vehicle-treated mice.
348 Consistent with our prediction that GDCA induces chromatin changes, ATAC-seq
349 identified hundreds of genomic regions with differential accessibility between the brains of GDCA-
350 and vehicle-treated mice (Figs. 5C-D; Fig. S10A-B; Supplementary Table 11). 200 of the 204
351 differentially accessible peaks (98%) were less accessible in the GDCA-exposed brains.
352 Moreover, using HOMER to annotate each differential peak with its nearest gene, we found that
353 six of the "nearest genes" were also differentially expressed in RNA-seq (Supplementary Table
354 11). This set of six genes included several known stress-response genes: *Ddit4*[85], *Errfi1*[91], *Rhob*[92],
355 and *Sgk1*[93]. For all six genes, the direction of change was concordant across datasets - decreased
356 expression of the gene and decreased accessibility of the nearby peak - providing compelling
357 evidence that the strong transcriptional changes induced by GDCA are driven, at least in part, by
358 chromatin remodeling.
359 We further annotated the differentially accessible peaks based on overlapping genomic
360 features and compared the proportion of peaks in each category to the proportions expected from
361 the reference genome. This analysis revealed enrichment of differential peaks in promoters and
362 introns (Fig. 5E; Fig. S10C; Supplementary Table 11). Promoters and introns frequently harbor
363 regulatory elements such as enhancers[94]; therefore, the enrichment of these features among
364 differential peaks further supports a direct link between GDCA-induced changes in chromatin
365 accessibility and effects on gene expression. Consistent with this interpretation, 4 of the 5 most
366 significantly differential intronic peaks fully overlapped elements annotated as distal enhancers in
367 the ENCODE SCREEN database (https://screen.wenglab.org/)[95].
368 Promoters and enhancers commonly contain motifs that bind transcription factors (TFs)
369 critical for the regulation of gene expression. We therefore used chromVAR[96] to assess whether
370 GDCA altered the accessibility of any TF motifs from the "CORE" collection of the well-established
371 JASPAR[97] database. We found that TF motif accessibility patterns quantified by chromVAR
372 clearly separated GDCA-exposed brains from controls (Fig. S11A). The TF motif with the highest
373 variability across samples was MA0007.4, which is recognized by the *Ar* transcription factor that
374 coordinates the cellular response to androgens (Fig. 5F; Supplementary Table 11). This *Ar* motif
375 was consistently less accessible in the GDCA-exposed brains than in controls (Fig. S11B).
376 A recent study showed that certain microbiome-derived bile acids, which share the sterol
377 structure of androgens, can antagonize the human androgen receptor[98]. Thus, GDCA may block
378 mouse *Ar* from nuclear translocation and binding to its target motifs, thereby reducing motif
379 accessibility - since TF binding usually opens chromatin[99] - and suppressing androgen-responsive
380 transcription. Consistent with this model, several of the genes strongly downregulated by GDCA
381 (e.g., *Adamts1*, *Akap12*, *Sgk1*) belong to the "Androgen Response" hallmark gene set from
382 MSigDB. GSEA likewise showed negative enrichment of this gene set (normalized enrichment
383 score = -2.17; Supplementary Table 8), although this did not reach statistical significance after

multiple testing correction (raw p = 0.05, adjusted p = 0.16), possibly reflecting a lag between certain chromatin changes and downstream transcriptional effects.

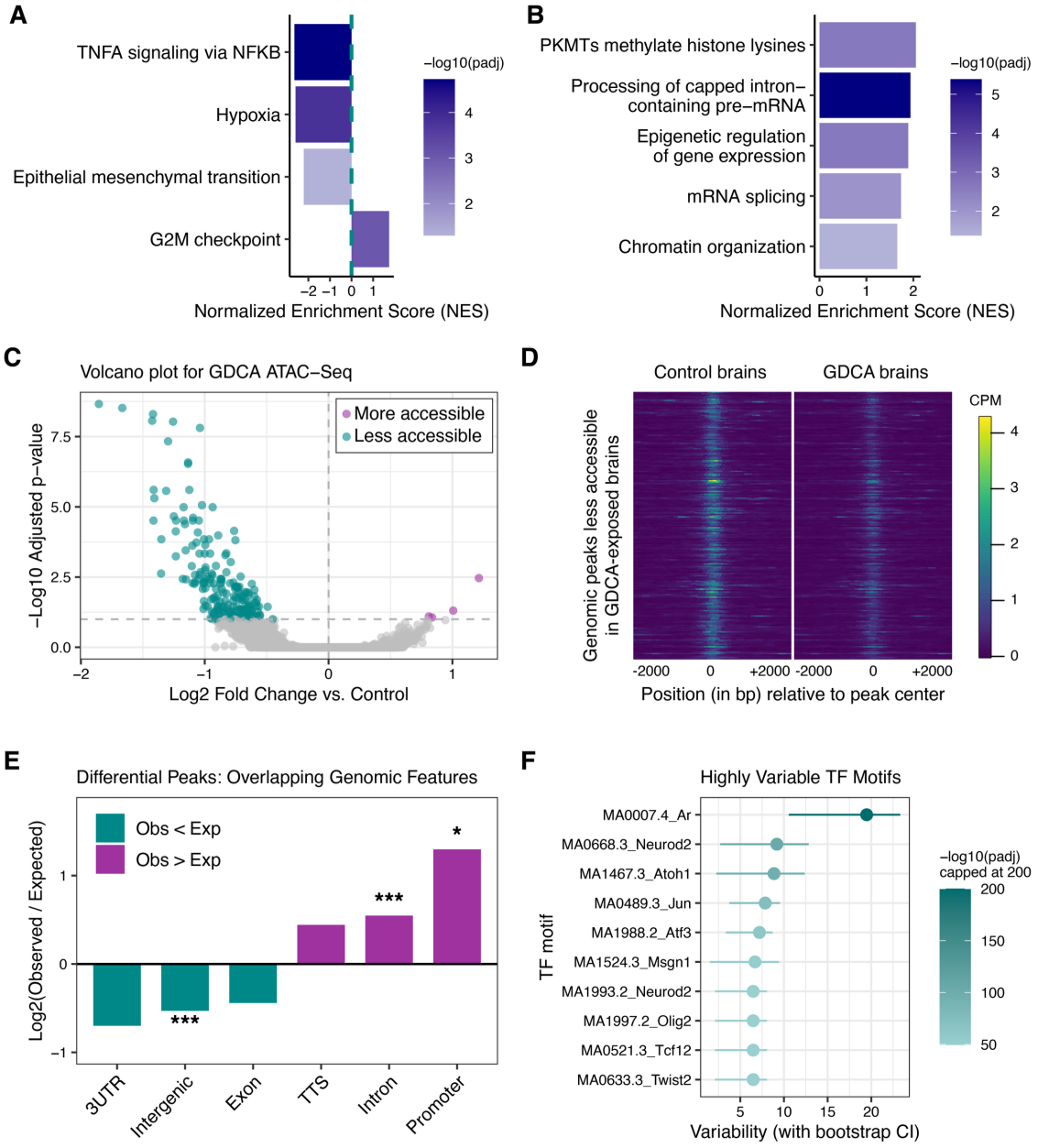

Fig. 5. GDCA suppresses stress-response genes and remodels chromatin in the brain. **(A)** All significantly enriched terms from gene set enrichment analysis (GSEA) based on hallmark gene sets; full results in Supplementary Table 8. **(B)** All significantly enriched terms from GSEA using the REACTOME pathway database; full results in Supplementary Table 8. **(C)** Volcano plot of differential chromatin accessibility between GDCA-treated and vehicle control mouse brains, based on ATAC-seq of flash-frozen right hemispheres from the initial RNA-seq cohort (see Methods). Y-axis: -log10(adjusted p-value) from DESeq2; x-axis: log2FoldChange vs. vehicle control. Purple dots represent genomic peaks with higher accessibility in brains from GDCA-exposed mice (adjusted $p \leq 0.1$ and positive log2FoldChange). Teal dots represent genomic

397 peaks with lower accessibility in brains from GDCA-exposed mice (adjusted $p \leq 0.1$ and negative
398 log2FoldChange). **(D)** Coverage heatmap for the 200 genomic peaks that were significantly less
399 accessible in brains from GDCA-exposed mice, vs. control. Each row represents one peak. BAM
400 files for individual brains within each condition were merged prior to visualization (Methods). CPM
401 = counts per million. **(E)** Observed versus expected proportions of differentially accessible peaks
402 overlapping various genomic features. Expected proportions were calculated based on the
403 reference genome. Introns and promoters are significantly enriched among differential peaks,
404 whereas intergenic regions are depleted. The symbol * indicates $p < 0.05$ and *** indicates $p <$
405 0.001. *p*-values were calculated by HOMER using a one-sided binomial test (upper-tailed when
406 observed > expected and lower-tailed when observed < expected). **(F)** Transcription factor (TF)
407 motifs with the highest variability in accessibility across ATAC-seq samples, as quantified by
408 chromVAR[96]. Dots represent point estimates of motif variability and horizontal lines indicate the
409 corresponding 95% bootstrap confidence intervals. The color scale shows the significance of
410 variability as -log10(adjusted *p*-value from chromVAR). To facilitate visualization, -log10(padj)
411 values were capped at 200; the true padj for the variability of MA0007.4_Ar across samples is 0.

412 GDCA acutely reduces mobility

413 Growing evidence indicates that androgens support both cognitive and motor function[100–102]. In
414 addition, increased chromatin accessibility can be beneficial for cognitive function[103], in stark
415 contrast to the accessibility reductions observed after GDCA treatment. Therefore, we
416 hypothesized that GDCA impairs cognitive and motor performance and may also influence
417 additional aspects of mouse behavior.

418 To test this, we first administered GDCA for three days (0.4 mg/kg/day, intravenous retro-
419 orbital injection) and assessed behavior (Fig. 6A). There were no detectable differences between
420 GDCA- and vehicle-treated mice, as assessed in an activity chamber on day 4 or in a Y-maze on
421 day 5 (n=15 male mice per group; see Figs. 6C-E, 6G-H, and Supplementary Table 12). We
422 reasoned that the administered GDCA would likely be cleared by the day of testing (e.g., via
423 hepatic uptake[104]), such that systemic levels were no longer elevated. Therefore, in a second
424 mouse cohort, we evaluated the impact of acute exposure (Fig. 6B). Here, GDCA was
425 administered via oral gavage, because retro-orbital injection, which is invasive, is not compatible
426 with same-day behavioral testing. Gavage doses (10 or 50 mg/kg) were based on prior mouse
427 studies evaluating GDCA's impact on obesity and ovarian function[105,106], and previous estimates
428 that only a small percentage (5-10%) of bile acids escape the enterohepatic circulation[107,108].

429 One hour after administration of GDCA or vehicle, mice were tested in the Y-maze. Like
430 vehicle-treated mice, GDCA-treated mice alternated between maze arms above chance levels
431 (Fig. 6F), indicating no impairment in spatial working memory. However, GDCA reduced mobility
432 in a dose-dependent manner, as evidenced by fewer entries into maze arms and lower total
433 distance moved within the Y-maze (Figs. 6I-L; Supplementary Table 12). At 50 mg/kg GDCA, the
434 mobility reduction was accompanied by a reduction in core body temperature (Fig. 6B and 6M).
435 Total distance moved also trended towards a GDCA-induced reduction within the setup of cohort
436 1 (p=0.054; Fig. 6H; Supplementary Table 12).

437 Although this cannot be formally established from the current data, the concurrent
438 decreases in mobility and body temperature following oral GDCA administration suggest a
439 centrally mediated response, as specific populations of neurons in the pre-optic area of the

hypothalamus have been shown to jointly regulate locomotion and thermoregulation in mice[109,110]. In addition, elevated plasma GDCA has been associated with Parkinson's Disease[26], a disorder that primarily involves the central nervous system and is characterized by both impaired locomotion[111] and a reduced mesor (rhythm-adjusted mean) of core body temperature[112].

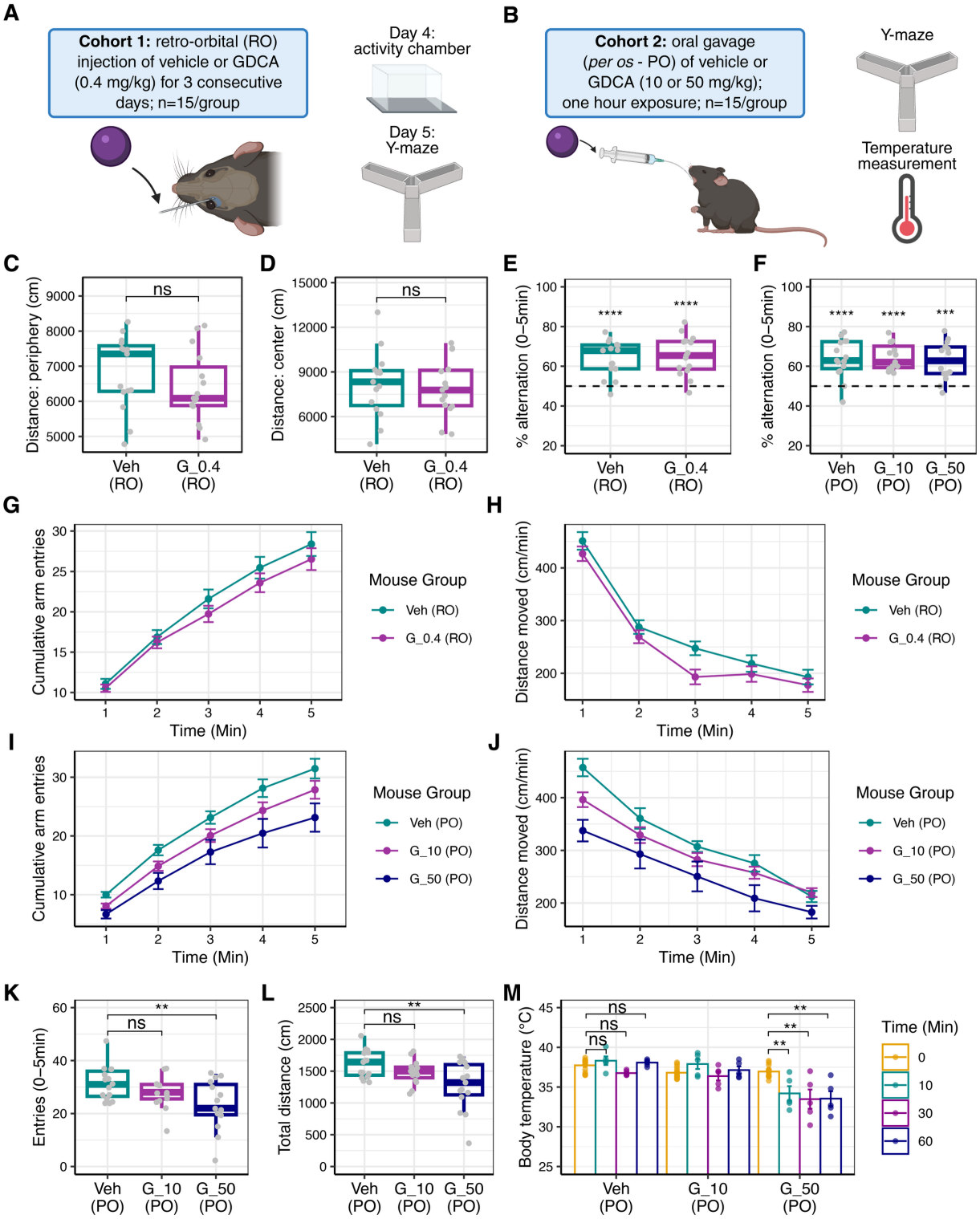

Fig. 6. GDCA acutely reduces mobility. **(A)** Schematic depicting the initial behavioral experiments

performed. There were *n*=15 mice per group, yielding *n*=30 mice total in this first behavioral cohort. **(B)** Schematic depicting the second set of behavioral experiments. There were *n*=15 mice per group, yielding *n*=45 mice total in this second behavioral cohort. Core body temperature was also measured in this cohort. **(C)** Total distance moved in the periphery of the activity chamber (cohort 1). Groups were compared using Welch's two-sample, two-sided *t*-test. **(D)** Same as (C), but for total distance moved in the center of the activity chamber. **(E)** Percent alternation between maze arms over the 5-minute duration of the Y-maze test (cohort 1). An alternation occurs when, after exiting one maze arm, the mouse does not enter one of the two arms they just visited, but rather enters the novel arm. Alternation percentages are defined as 100% * (number of alternations) / (total number of opportunities to alternate). Statistics compare the alternation percentages within each group to the chance level (50%[113,114]), using Welch's one-sample, two-sided *t*-test. **(F)** Same as (E), but for cohort 2. One mouse from the G_50 group was excluded as it had less than three arm entries and thus had no opportunities to alternate. **(G)** Cumulative entries into the arms of the Y-maze (cohort 1). **(H)** Distance moved within the Y-maze, minute-by-minute (cohort 1). **(I)** Same as (G), but for cohort 2. **(J)** Same as (H), but for cohort 2. **(K)** Boxplot of the data from minutes 0-5 in panel (I). Groups were compared using one-way ANOVA with Dunnett's post-hoc test. **(L)** Boxplot depicting the total distance traveled in the Y-maze by cohort 2, calculated as the sum of the values underlying panel (J). Statistics as in (K). **(M)** Core body temperature (°C) in cohort 2 measured at 0, 10, 30, and 60 min after gavage, six days after Y-maze testing. Bars show mean ± SEM. All *n*=15 mice per group were measured at time 0; *n*=5 mice per group were measured at each subsequent timepoint. Within each treatment group, time effects were assessed using one-way ANOVA; when significant, Dunnett's posthoc test was also applied (statistics shown). In all panels, ns indicates not statistically significant, * indicates $p \leq 0.05$, ** indicates $p \leq 0.01$, *** indicates $p \leq 0.001$, and **** indicates $p \leq 0.0001$. In all boxplots, boxes represent the interquartile range (IQR), the horizontal line indicates the median and whiskers extend between (25th percentile - 1.5*IQR) and (75th percentile + 1.5*IQR).

Discussion

The gut microbiome produces and impacts the systemic concentration of hundreds of metabolites, each of which may profoundly influence host organs, including the brain. However, systematic, high-throughput efforts to identify metabolites relevant to gut-brain signaling are lacking, partly because testing hundreds of molecules in animal models - the most accurate system to assess brain effects - is impractical. In this study, we integrated computational, *in vitro*, and *in vivo* approaches to identify age-related, microbiome-derived blood metabolites that - at physiologically relevant levels - induce significant molecular changes in the mouse brain. Among other changes, we observed impacts on RNA splicing and chromatin accessibility, whose dysregulation is implicated in brain aging and in age-related neurodegeneration[73,115,116]. Furthermore, we found that a microbiome-derived secondary bile acid, GDCA, can reduce mobility, a function that declines with aging and neurodegenerative disease. These findings demonstrate that "microbiome aging" may substantially contribute to "brain aging" through impacts on the blood metabolome, and that targeting the microbiome and its metabolites may offer cognitive benefits during aging.

The aminoxide TMAO has been extensively studied in the context of cardiovascular disease[13,117], and there is a growing body of research on its impact on the brain, where it has been shown to induce mitochondrial dysfunction, oxidative stress, neuroinflammation, and reductions in synaptic plasticity[34,58]. We found that TMAO also upregulates the glycolytic pathway in the brain - perhaps to compensate for mitochondrial dysfunction - and impacts RNA splicing by inducing strong downregulation of splicing factors and driving dozens of differential splicing events. Although prior work has identified splicing changes in the brains of germ-free vs. conventionally raised animals[118], to our knowledge, this is the first demonstration that specific microbiome-derived metabolites can alter host splicing patterns - whether in the brain or in any other host organ. GDCA may also affect splicing (Fig. 5B), raising questions about the relative impacts of each individual microbiome-derived blood metabolite and how these impacts might converge to influence normal brain function and the development of brain pathologies.

Unlike TMAO, little is known about the effects of GDCA on the mammalian nervous system, with prior knowledge limited to its association with neurodegenerative disease and cognitive impairment in several human cohorts[24–28]. Here, we build upon this knowledge, finding that GDCA alters chromatin accessibility, which might be the mechanism by which it also silences genes required for stress and injury response in the mouse brain. Large microbiome perturbations, such as antibiotics and germ-free status, have been shown to impact the brain epigenome[119]; however, previous metabolite-specific work has focused on the impact of short-chain fatty acids[120], leaving open questions about the many other classes of microbial effectors, including bile acids.

Our data suggest that GDCA substantially alters the brain transcriptome and epigenome, largely by antagonizing the host androgen receptor. This may suppress host androgen signaling, a pathway that is generally considered beneficial for cognitive and motor function[100–102]. This hypothesis aligns with our finding that GDCA exposure induces mobility deficits. However, further study - with varied dosing and testing paradigms - will be required to fully elucidate the cognitive and motor impacts of GDCA.

Although our work clearly demonstrates that circulating microbiome-derived metabolites can induce significant molecular alterations in the brain, it has several limitations. First, we tested only short-term exposures. However, brain aging and neurodegeneration occur over long periods of time. It will thus be important to decipher the short- vs. long-term effects of metabolites of interest. *In vitro*, this may require determining the half-life of each metabolite and ensuring continuous exposure to the desired concentration. *In vivo*, metabolites may need to be administered via osmotic minipump or through the diet. To determine the most physiologic dosing regimens, pharmacokinetic (PK) studies - involving metabolomics at various timepoints - will be necessary. Indeed, even the limited effects of *acute* exposure to PA and IAA in our study (Fig. 3B) may simply reflect suboptimal bioavailability of the administered formulations, underscoring the value of PK studies.

Another limitation is that, while our results show that TMAO increases the expression of glycolytic enzymes, both *in vitro* and *in vivo*, we did not definitively establish changes in glycolytic flux. This can be investigated using ^{13}C isotope tracing or similar approaches. Additionally, while we find interesting molecular phenotypes in adult mice, these results may or may not translate to aged animals. Future *in vivo* work in aged mice will be informative, in this regard, given that age may modify the brain's response to each metabolite. Relatedly, age-related comorbidities such as diabetes and cardiovascular disease may impact host response to individual metabolites, highlighting the importance of testing metabolite effects in the relevant disease models. Finally, because our multi-omic analyses were conducted using bulk rather than single-cell methods, the cell-type-specific effects of TMAO and GDCA remain unclear.

Despite these limitations, our work underscores that the gut microbiome, which is potentially modifiable, is a valuable therapeutic target in the context of brain aging. We identify specific age-associated microbiome metabolites that impact the transcriptional and epigenetic landscape of the brain, with likely consequences for brain function, as demonstrated by the observed impact of GDCA on locomotion. In addition, although we focused on brain aging in this work, the framework we describe - beginning with metabolomics data analysis, followed by *in vitro* transcriptomic screening, and concluding with *in vivo* studies of host organs and behavior - can be applied to identify the microbiome metabolites relevant to any host pathology of interest, providing a powerful tool for the field of microbe-host interactions.

Methods

Identifying microbiome-associated metabolites whose blood levels change with age

To identify metabolites whose blood levels change with aging, we leveraged data from three large cohort studies[18–20] listed in a recent review[17] on the metabolomics of aging. From Menni *et al.*[18], we retained all metabolites from Table S2, since only metabolites significantly associated with age were included in this table. From Dunn *et al.*[19], we retained metabolites with p adj <= 0.05 under the test labeled "_age.g2" in Supplementary Material 2 ("AGE" tab). From Darst *et al.*[20], we retained metabolites with p_age <= 0.05 in Table S1.

Separately, we curated a list of 329 human-associated metabolites that have been reported to be produced by microbes and/or are the products of host-microbe cometabolism. To create the list, we first downloaded Table S3 from a recent study on interactions between human-associated metabolites and GPCRs[21], and filtered to metabolites that included "Bacteria" in the "Source" column. After filtering, there were 320 metabolites. We then added the following nine metabolites known to be microbially producible and/or producible through host-microbe cometabolism[23,121–124]: acetic acid, butyric acid, indole-3-carboxaldehyde, indolelactic acid, enterolactone, imidazole propionate, p-cresol sulfate, hippuric acid and indoleacetic acid.

Then, we intersected the age-associated metabolites from each study with the curated list of metabolites associated with microbial metabolism. The intersection method was different per study given the differing formats of the tables. Specifically, for Darst *et al.*, we were able to intersect based on HMDB ID. We also noted that there was one metabolite that matched on CAS number but not on HMDB ID, given that it was listed as "ornithine HCl" in our curated list of microbiome-associated metabolites, but simply "ornithine" in the Darst study. So, we added ornithine manually to the intersection output. For the Menni and Dunn datasets, which lacked standardized identifiers, we used fuzzy string matching (via the Python package fuzzywuzzy, v0.18.0) to identify metabolites with similar names, followed by manual curation to confirm true matches. We also added two intersecting metabolites that were missed by fuzzy matching - indoleacetate and hippurate.

This process yielded 114 overlapping metabolites, 79 of which were unique based on HMDB ID. To narrow the list to metabolites most strongly associated with the gut microbiome, we leveraged two additional resources: **(1)** a recent study comparing blood metabolite levels between germ-free and conventionally raised mice[12]; and **(2)** the GUTSY Atlas[22], which reported the proportion of variance in blood metabolite levels "explained" by the gut microbiome for 1,168 metabolites based on paired stool-blood data for over 8,000 humans. Metabolites were retained for the final panel if they met at least one of two criteria: **(1)** showed significantly different blood levels between germ-free and conventionally raised mice[12]; **(2)** ranked in the top 20% of blood metabolites for the GUTSY variance-explained metric. We eliminated alanine and uridine, the former due to its minimal expected impact on cellular processes[29], and the latter because its blood levels increased with age in one study[18] but decreased with age in another[20].

587 The final table of 30 metabolites and their properties is contained in Supplementary Table
588 1. The table also specifies the exact product that was ordered for testing in the *in vitro*
589 transcriptomic screen.
590 Of note, at a later date, after conducting the *in vitro* RNA-seq experiments, we discovered
591 that the p_age values in Table S1 of the Darst study had not been corrected for multiple
592 hypothesis testing. However, even after we manually corrected for multiple hypothesis testing
593 (using a False Discovery Rate approach in R v4.3.2), all the metabolites from the Darst study in
594 our final panel maintained significance using an FDR threshold of padj ≤ 0.1, with all but cholate
595 (padj = 0.065) and glycodeoxycholate (padj = 0.061) also having a padj ≤ 0.05.

596 Cell culture

597 Human cerebral microvascular endothelial cells (hCMEC/D3; Sigma, Cat #SCC066) were
598 obtained as a gift from the lab of Prof. Mark Kay at Stanford University. Cell line authentication
599 was conducted using the ATCC Human Cell STR Profiling Service at passage #9 in October
600 2023, prior to initiating the experiments described in this manuscript. Cultures were maintained in
601 a 37°C, 5% CO_2 incubator at passage numbers ≤ 22, well below the limit of 35 established by the
602 developers of the cell line[31]. The cell medium was prepared from the EGM2-MV BulletKit (Lonza,
603 Catalog #CC-3202). The VEGF supplement was excluded from the medium based on literature
604 precedent[58,122] and due to VEGF's ability to impair the key barrier-forming properties of the
605 cells[125]. Cells were passaged every two days and were maintained on tissue culture-treated
606 plates. Cells were tested for mycoplasma contamination at six-month intervals during periods of
607 active culture using the ATCC Universal Mycoplasma Detection Kit (ATCC, Cat #30-1012K).

608 *In vitro* transcriptomic screen - experimental details

609 The screen was conducted in four separate batches using 12-well plates. Prior to cell seeding,
610 each well was coated with 0.5ml of a 1:20 dilution of rat tail collagen (Sigma, Catalog #08-115) in
611 DPBS (Fisher, Catalog #MT21031CV). Collagen was incubated on the plates at 37°C for 1 hour
612 and rinsed off twice with DPBS before cell seeding. Cells were seeded at passages #9-10, at a
613 density of 100,000 cells per well. Seeded cells were grown for six days prior to treatment, based
614 on prior literature[58,122]. The cell culture medium was refreshed every two days.
615 Each 12-well plate was organized to include three wells for vehicle controls and nine wells
616 for testing three metabolites, with three biological replicates per metabolite. All metabolites tested
617 on a given plate were dissolved in the same solvent (H_2O or DMSO) and vehicle controls included
618 an equivalent volume (1%) of the solvent in the final media used for the assays. Because urate
619 was insufficiently soluble in H_2O or DMSO alone, the final treatment media for this metabolite
620 included a small percentage (approximately 0.1%) of NaOH in addition to 1% H_2O.
621 Each batch consisted of three 12-well plates, which allowed room for testing nine
622 metabolites per batch. To allow for inclusion of an LPS control condition per batch, eight candidate
623 metabolites were tested per batch. Specifically, batches #2-4 tested 8 metabolites each and batch
624 #1 tested 6, to cover the entire set of 30 metabolites (see Supplementary Table 3). Cells were
625 treated with a metabolite, vehicle, or LPS for 3h before being harvested in TRIzol and stored at -
626 20°C for downstream RNA extraction and sequencing.

627 For each metabolite, we determined a physiologically relevant concentration to add to
628 cells (Supplementary Table 1), primarily based on information listed in the Human Metabolome
629 Database (HMDB) as of November 2023. Specifically, for each metabolite, we searched for the
630 metabolite in HMDB, clicked the "Concentrations" tab of the relevant entry, examined the
631 concentrations listed for "normal" adult blood samples, and selected a concentration based on
632 those listings. HMDB did not provide blood concentrations for four metabolites:
633 glycodeoxycholate, imidazole propionate, methyl indole-3-acetate, and N-acetyl-L-alanine. For
634 glycodeoxycholate, we chose the concentration based on Table S2 of Qing *et al.*, *Schizophrenia*
635 2022[126]. For imidazole propionate, a relevant physiological concentration was determined based
636 on Fig. 1 of Molinaro *et al.*, *Nature Communications* 2020[121]. For methyl indole-3-acetate, we
637 were not able to find literature on the exact concentrations in adult blood samples. We tested 1μM
638 because it was between previously reported concentrations of the metabolite in adult urine[127] and
639 the chosen test concentration of the related metabolite indole-3-acetate. For N-acetyl-L-alanine,
640 we tested 3μM based on previous literature that included *in vitro* experiments with this metabolite
641 (Yang *et al.*, *Int J Mol Sci* 2023; Section 2.2[128]).
642 RNA was extracted using the following protocol. Samples were thawed to room
643 temperature and incubated for an additional five minutes after thaw. 200μl chloroform was then
644 added per 1ml of TRIzol used; then, samples were briefly vortexed and incubated 2-3 minutes at
645 room temperature, prior to a 15-minute centrifugation at 17,000 x g at 4°C. The aqueous phase
646 was transferred to a new tube. Steps 2-7 of the "Part 1" quick-start protocol for the RNeasy Mini
647 Kit (Qiagen, Catalog #74106) were then executed, skipping the on-column DNase digestion but
648 including the optional dry spin. DNase digestion was conducted using TURBO DNase (Fisher
649 Scientific, Catalog #AM2239). Then, the "RNA cleanup" section of the RNeasy Mini handbook
650 was executed, using 2 minutes rather than 1 minute for the dry spin. Finally, an ethanol
651 precipitation was conducted for all samples to clean up any ethanol contamination, based on the
652 relevant protocol from Cold Spring Harbor Laboratories[129]. RNA samples were sent to Novogene
653 for quality control, mRNA library preparation (poly A enrichment), and sequencing (NovaSeq
654 6000, 150bp paired end reads, 6Gb raw data per sample).

655 *In vitro* transcriptomic screen - computational analysis

656 Computational analysis of the *in vitro* RNAseq data was performed separately for each
657 sequencing batch, as follows. First, FASTQ files from Novogene were trimmed to remove adapter
658 and low-quality bases using TrimGalore v0.6.10 with the following parameters: -q 30 --fastqc --
659 stringency 3 --max_n 15 --output_dir trimming_out --cores 2 --retain_unpaired --paired
660 <SAMPLE>_1.fq.gz <SAMPLE>_2.fq.gz.
661 Trimmed paired reads were pseudoaligned to the human reference transcriptome using
662 kallisto v0.48.0[130]. The reference transcriptome was downloaded from Ensembl (release 110,
663 Homo_sapiens.GRCh38.cdna.all.fa.gz) and an index was built using the kallisto index command.
664 For pseudoalignment, the kallisto quant command was used with the -b 100 option, corresponding
665 to 100 bootstraps.
666 Samples were then grouped based on the solvent included in the media (DMSO or H_2O),
667 and a principal component analysis (PCA) was performed separately for each solvent group, as
668 follows. First, transcript abundance tables generated by kallisto were normalized and filtered using
669 the kallisto_table function from the sleuth R package (v0.30.2), using the options normalized =

670 TRUE and use_filtered = TRUE. The resulting tables were log-transformed using the natural
671 logarithm of (x+0.5) prior to PCA, which was conducted using the prcomp function in R v4.3.2.
672 PCA plots were used to identify potential outlier samples within each group - defined as
673 samples positioned far from: (1) the vast majority of samples in the plot, and (2) the other
674 replicates within their treatment condition. Due to the subjective nature of visual outlier
675 identification, samples were only excluded from downstream analyses if their removal was
676 additionally supported by deviant quality control (QC) statistics from Novogene. **Note:** The PCA
677 plots for each sequencing batch are displayed in Figs. S4 and S5, and the corresponding sample
678 lists and QC statistics are contained in Supplementary Table 3.
679 Based on the above criteria, the following 5 (out of 138) samples were excluded from
680 downstream analysis. From batch 2, oxalate replicate #1 and carnitine replicate #2 were removed
681 (supporting QC statistic: low %GC content compared to the other samples in the batch). From
682 batch 3, glycodeoxycholate replicate #1 and quinolinate replicate #2 were removed (supporting
683 QC statistic: low %GC content compared to other samples in the batch). From batch 4 - DMSO
684 control replicate #5 was removed (supporting QC statistic: low RNA concentration compared to
685 all other DMSO control samples).
686 Following PCA and outlier removal, DESeq2[131] v1.42.1 was used to determine
687 differentially expressed genes between each set of metabolite-treated samples and the
688 corresponding vehicle controls in the sequencing batch, using the default significance cutoff of
689 alpha=0.10. As specified in Supplementary Table 3, the number of vehicle controls per solvent
690 per sequencing batch ranged from three to nine. Gene abundance values were determined from
691 the per-transcript kallisto outputs using tximport (v1.31.0). When applicable, the corrplot R
692 package (v0.95) was used to verify that all vehicle controls of the same solvent (e.g., 1% DMSO
693 controls) on different plates could be grouped, based on strong correlations - Pearson's $r > 0.98$
694 - of log-transformed gene abundances.
695 As recommended by the DESeq2 developers, the function lfcShrink[63] was applied to
696 conservatively shrink log2foldchanges, using the shrinkage estimator 'apeglm.' Additionally, to
697 avoid overcounting the number of significant hits per metabolite, we filtered the DESeq2 output of
698 differentially expressed genes to eliminate lines that were exact duplicates of previous lines
699 besides the Ensembl ID field, which can occur when two different Ensembl gene IDs are mapped
700 to the same physical gene. Finally, genes with an absolute shrunken log2 fold change ≤ 0.1 were
701 not counted as DEGs, even if they met the significance threshold of adjusted $p \leq 0.1$.
702 The KEGG pathway enrichment analyses shown in Figs. 2B and S2 were conducted using
703 g:Profiler (https://biit.cs.ut.ee/gprofiler/gost)[132] on August 17, 2025 using the default g:SCS
704 significance threshold and a custom list of background genes - specifically, all genes that passed
705 DESeq2's internal filters in the corresponding DESeq2 analysis. For the analysis of DEGs in the
706 Alzheimer and Parkinson's KEGG pathways (Fig. 2C), the pathway gene lists were retrieved on
707 July 19, 2025 from https://rest.kegg.jp/link/hsa/path:hsa05010 and
708 https://rest.kegg.jp/link/hsa/path:hsa05012, respectively. The numbers reported in Fig. 2C
709 represent numbers of unique genes (based on Entrez ID).

710 *In vitro* cytotoxicity testing

711 hCMEC/D3 cells (passage #22) were seeded on Day 0 at a density of 100,000 cells per well in
712 12-well plates. Prior to seeding, each well was coated with 23µg rat tail collagen (Sigma, Cat.

713 #08-115) in 1mL DPBS (Fisher, Catalog #MT21031CV) and rinsed twice with DPBS following a
714 10-minute incubation at room temperature.
715 On Day 2, cells were treated for 3 hours with EGM2-MV BulletKit medium (Lonza, Catalog
716 #CC-3202) excluding the VEGF supplement and supplemented with either: **[1]** metabolites at the
717 concentrations shown in Fig. S7, **[2]** vehicle control (i.e., 1% DMSO or 1% H_2O), or **[3]** 20%
718 DMSO (cytotoxic control).
719 Following treatment, cells were detached with 0.05% trypsin-EDTA (Fisher Scientific,
720 Catalog #25-300-054), pelleted by centrifugation (100 x g, 5min, 4°C), and resuspended in 150µl
721 serum-free, phenol red-free EGM2-MV medium (basal medium: Lonza, Catalog #CC-3129;
722 supplements: Lonza EGM2-MV SingleQuots kit, Catalog #CC-4147, excluding FBS and VEGF).
723 30µl of Propidium Iodide ReadyFlow reagent (Thermo Fisher, Catalog #R37169) was added to
724 the suspension, and fluorescence was measured using a NovoCyte Quanteon flow cytometer at
725 the Stanford Shared FACS Facility.

726 Animals

727 Male C57BL/6 mice (3 months old) were obtained from Jackson Laboratories (stock # Jax
728 000664). All mice were kept on a 12 h-12 h light-dark cycle and provided *ad libitum* access to food
729 and water. All animal care and procedures complied with the Animal Welfare Act and were in
730 accordance with institutional guidelines and approved by the institutional administrative panel of
731 laboratory animal care at Stanford University (PIs of animal protocols: T. Wyss Coray, M.
732 Shamloo; protocol #s 29100 and 18466).

733 Mouse brain transcriptomics after metabolite injection

734 Guided by prior studies investigating TMAO and the microbiome metabolite p-Cresol sulfate[58,122],
735 we conducted bulk transcriptomics on mouse half-brains following a 2-hour exposure to each
736 metabolite of interest or the corresponding vehicle control. As detailed in Figs. #2-3 and the
737 accompanying text, four metabolites were tested in mice - palmitic acid (PA), indoleacetic acid
738 (IAA), trimethylamine N-oxide (TMAO), and glycodeoxycholic acid (GDCA). Intravenous retro-
739 orbital injection under isoflurane anesthesia was used as the administration route.
740 Metabolite dosing was based on precedent from the study on TMAO that guided
741 experimental design[58]. For TMAO (Cayman Chemicals, Item #17354, Batch #0522898-67), we
742 used the same dose as the original study, 1.8 mg/kg. This dose was described as "calculated to
743 approximate human circulating TMAO levels." Thus, for the remainder of the metabolites, we
744 examined the targeted metabolomics literature[26,28,48–55] to identify the range of circulating levels
745 previously observed in human seniors, and calculated mouse-equivalent doses of observed
746 human concentrations, using well-established guidelines[56,57]. PA (Sigma, Catalog #P0500-10G,
747 Lot #0000253065) was administered at a final dose of 22.2 mg/kg (~100µM total body dose). IAA
748 (Sigma, Catalog #I2886-5G, Lot #0000249926) was administered at a final dose of 1.5 mg/kg
749 (~10µM total body dose). GDCA (Sigma, Catalog #361311-5GM, Lot #4045885) was
750 administered at a final dose of 0.4 mg/kg (~1µM total body dose).
751 Two experiments were conducted in total. **Experiment 1** contained 8 mice; 4 mice
752 received 1.8 mg/kg TMAO in 100µl saline, and 4 mice received 100µl saline (vehicle control).
753 **Experiment 2** contained 20 mice, in two groups. Group 1 contained 8 mice; 4 mice received 0.4

754 mg/kg GDCA in 100µl saline, and 4 mice received 100µl saline (vehicle control). Group 2
755 contained 12 mice; 4 mice received 22.2 mg/kg PA in 100µl saline containing 6% DMSO, 4 mice
756 received 1.5 mg/kg IAA in 100µl saline containing 6% DMSO, and 4 mice received 100µl saline
757 also containing 6% DMSO (vehicle control). ***Note:*** unlike TMAO and GDCA, PA and IAA are only
758 soluble in organic solvents such as DMSO, hence the use of DMSO above.
759 For sacrifice, mice were anesthetized using 2.5% Avertin (v/v). As per the original TMAO
760 study[58], mice were transcardially perfused with 0.9% saline after sacrifice and prior to brain
761 removal, in order to remove contaminating blood. Forceps used for brain extraction were pre-
762 treated with RNaseZap (Thermo Fisher, Catalog #AM9780) and subsequently rinsed twice with
763 RNase-free water to minimize the risk of RNA degradation. Brains were sagittally hemisected at
764 the corpus callosum prior to storage. Left hemispheres were stored in 1ml RNAlater overnight at
765 4°C, and then dabbed on a Kimwipe to remove excess RNAlater before transfer to a fresh tube
766 for storage at -80°C. Right hemispheres were either processed in the same manner or flash-
767 frozen directly at -80°C. Specifically, for the TMAO-treated and corresponding vehicle control
768 brains - which were part of the first experiment performed - the right hemispheres were processed
769 identically to the left. In the second experiment, however, the right hemispheres were flash-frozen
770 at -80°C without RNAlater incubation.
771 RNA was extracted from frozen left hemispheres using a modified version of the protocol
772 from the QIAWave RNA Mini Kit (Qiagen, Catalog #74536), as follows. A bead beater (Qiagen
773 Tissue Lyser II) was used to homogenize the left hemisphere in a collection microtube (Qiagen
774 Catalog #19560) containing 700µL of pre-chilled QIAzol (Qiagen, Catalog #79306) and stainless
775 5mm steel bead (Qiagen Catalog #69989). For bead beating, the tube was positioned in between
776 cold metal blocks prechilled at -20°C. Samples were homogenized at 30Hz for five minutes, kept
777 on ice for 1 minute, then homogenized at 30Hz for an additional 2 minutes. Following
778 homogenization, the tube was incubated at room temperature for 3-5 minutes. 200µL was then
779 set aside for RNA extraction in a DNA LoBind tube; the remaining volume was stored in a fresh
780 DNA LoBind tube at -80°C. 500µL of additional QIAzol was added to the 200µL tube to make
781 700µL; then, all the liquid was transferred to a DNA LoBind tube containing 200µL chloroform.
782 The tube was capped and vortexed for 15 seconds, then incubated at room temperature for 2-3
783 minutes and centrifuged at 12,000xg for 15min at 4°C. 150µL x 2 times (300µL total) of aqueous
784 phase was then transferred to a DNA LoBind tube containing 300µL 70% ethanol. The tube was
785 then inverted 10 times to mix, and briefly centrifuged. ~600µl of sample was transferred to the
786 RNeasy Mini spin column, then spun at 10,000xg for 30 seconds at room temperature. Flow-
787 through was discarded, and 350µL RW1 was added to the column. The column was spun at
788 10,000xg for 30 seconds at room temperature, and the flow-through was again discarded. 500µL
789 RPE was added to the column, and the column was spun at 10,000xg for 30 seconds at room
790 temperature, after which flow-through was discarded. The preceding RPE wash and spin was
791 then repeated for 2 minutes. The tube was then centrifuged at maximum speed for one minute at
792 room temperature. The column was transferred to a new 1.5ml DNA LoBind tube, to which 50µL
793 RNAse-free water was added. The lid was closed and the tube was incubated at room
794 temperature for 1-2 minutes. For elution, the tube was spun for one minute at 10,000xg at room
795 temperature. The same 50µL of eluate was used to repeat the previous step.

RNA samples were sent to Novogene for quality control, mRNA library preparation (poly A enrichment), and sequencing (NovaSeq 6000, 150bp paired end reads, 6Gb raw data per sample). A sample list and QC statistics are included in Supplementary Table 3.

Mouse brain transcriptomics - preliminary data analysis

The following steps were performed separately for each experiment defined above. First, FASTQ files from Novogene were trimmed to remove adapter and low-quality bases using TrimGalore v0.6.10 with the following parameters: --fastqc --stringency 3 --max_n 15 --output_dir trimming_out --cores 2 --retain_unpaired --2colour 30 --paired <SAMPLE>_1.fq.gz <SAMPLE>_2.fq.gz.

Trimmed paired-end reads were pseudoaligned to the standard mouse transcriptome index provided with the v1 release of kallisto[130], using kallisto v0.50.1. For pseudoalignment, the kallisto quant command was used with the -b 100 option, corresponding to 100 bootstraps.

Principal component analysis (PCA) was conducted using the following functions available in DESeq2 (v1.42.1): vst (setting blind = TRUE) and plotPCA. PCA revealed two key insights that guided subsequent decisions: (1) For experiment 1 - TMAO replicate #3 was positioned away from every other TMAO-treated sample along the first two components (Fig. S6A), necessitating further investigation of this sample prior to downstream analysis. (2) For experiment 2 - PCA revealed strong separation of samples by RNA extraction batch (Fig. S6B), necessitating the inclusion of this variable as a covariate in downstream differential expression analysis.

TMAO replicate #3 was ultimately excluded from subsequent analyses, including DESeq2 differential expression analysis, based on three additional facts beyond its placement in PCA. First, TMAO replicate #3 exhibited high leverage in the initial DESeq2 run; i.e., with TMAO replicate #3 included, it showed the highest mean Cook's distance, more than 1.5x that of any other sample, indicating a disproportionate influence on the linear model. Second, DESeq2 differential gene expression analysis comparing TMAO replicate #3 vs. all other samples revealed enrichment of blood markers (Hba-a1: $\log_2$FC = 2.28, padj = 3.9 × 10E-4; Hbb-bt: $\log_2$FC = 1.72, padj = 0.03; Supplementary Table 7), suggesting potential incomplete perfusion and/or other blood contamination. Third, excluding TMAO replicate #3 brought our differential expression results into closer agreement with those reported by Hoyles *et al.*[58], the study that inspired the design of this experiment, and with the broader literature on TMAO, strengthening confidence in the results.

DESeq2[131] v1.42.1 was used to determine differentially expressed genes between metabolite-treated samples and matched vehicle controls, using the default significance cutoff of alpha=0.10. For experiment 1, TMAO replicate #3 was excluded for the reasons detailed above, yielding *n*=3 TMAO brains and *n*=4 control brains for the final differential expression analysis. For experiment 2, all *n*=4 brains per condition were included in the final analysis, and the RNA extraction batch was included as a covariate, based on the PCA results described above (Fig. S6B). As recommended by the DESeq2 developers, the function lfcShrink[63] was applied to conservatively shrink log2foldchanges, using the shrinkage estimator 'apeglm.' All final DESeq2 differential gene expression results for PA, IAA, TMAO and GDCA are contained in Supplementary Table 7. Genes with an absolute shrunken log2foldchange ≤ 0.1 were not counted as DEGs, even if they met the significance threshold. All per-gene abundances for DESeq2 analysis were determined from the per-transcript kallisto outputs using tximport (v1.30.0).

Mouse brain transcriptomics - gene set enrichment analysis

Gene set enrichment analysis (GSEA) was conducted using the R package fgsea (v1.28.0). The relevant gene sets (hallmark gene sets and REACTOME pathways for mouse) were downloaded from https://www.gsea-msigdb.org/gsea/msigdb/mouse/collections.jsp on July 4, 2025. Enrichments with padj ≤ 0.05 were considered statistically significant.

Mouse brain transcriptomics - marker gene analysis

Marker genes for six different brain cell classes were determined using the following command in the R package Seurat (v5.3.0): FindAllMarkers(seurat_object, group.by = "ident", slot = “data”, only.pos = TRUE, min.pct = 0.25, logfc.threshold = 0.5). The resulting marker genes were further filtered to those with adjusted *p*-value ≤ 0.05. The Seurat object was constructed using single cell data from the mouse brain, specifically data from the 8 young mice (age-matched to those in our study) included in Ximerakis *et al.*, 2019[68]. Expression data, and metadata specifying the class of each cell, were downloaded from https://singlecell.broadinstitute.org/single_cell/study/SCP263/aging-mouse-brain on August 22, 2025.

Mouse brain transcriptomics - differential splicing analysis

Differential splicing events were identified using rMATS-turbo[74] (v4.1.1), as follows. First, STAR (v2.7.11b) was used to align trimmed paired-end reads to the mouse genome downloaded from GENCODE (Release M37, i.e., GRCm39). The following command was used: STAR --genomeDir <directory_containing_genome> --readFilesIn <SAMPLE>_1.trimmed.fq.gz <SAMPLE>_2.trimmed.fq.gz --outFileNamePrefix <SAMPLE> --outSAMunmapped Within --outSAMattributes NH HI AS NM MD XS --twopassMode Basic --alignSJDBoverhangMin 1 --alignSJoverhangMin 8 --runThreadN 16 --outSAMtype BAM SortedByCoordinate --outSAMstrandField intronMotif --readFilesCommand zcat.

The resulting bam files were then run through rMATS-turbo using the following command: rmats.py --gtf <path_to_genome_annotation_file> --b1 <file_specifying_saline_bams> --b2 <file_specifying_tmao_bams> --od <output_directory> --tmp <directory_for_tmp_files> -t paired --libType fr-unstranded --readLength 150 --variable-read-length --nthread 10 --cstat 0.1 --novelSS --allow-clipping. Based on the “JCEC” output files, this command initially nominated 126 differential splicing events between TMAO-treated and saline-treated brains (FDR ≤ 0.05), which we further narrowed to 44 using the following four filters: **(1)** ≥ 5 read counts on average per group, **(2)** exclusion of events with average PSI < 0.05 or > 0.95 in both groups, **(3)** FDR ≤ 0.01, and **(4)** ΔPSI ≥ 0.10.

The sashimi plot in Fig. S9A was generated using ggsashimi[133] (v1.1.5).

Bulk ATAC-seq of brains of GDCA-exposed vs. vehicle control mice

As described above under “Mouse brain transcriptomics after metabolite injection,” only the left hemisphere of each brain in these experiments underwent RNA-sequencing. The right hemispheres from GDCA-exposed and corresponding vehicle control mice were flash-frozen at -80°C, enabling ATAC-seq.

878 Mouse brain nuclei were isolated following procedures established for processing
879 mammalian brains[134] and then ATAC-seq was carried out as previously described[135] with some
880 modifications.
881 Briefly, dissected brain tissue was added to 1 mL nuclei extraction buffer (NEB: 250 mM
882 Sucrose, 65 mM B-glycerol, 1x protein inhibitor, 25 mM KCl, 5 mM MgCl2, 20mM HEPES-KOH,
883 0.5% IGEPAL CA-630, 1 mM DTT, 0.2 mM Spermine, 0.5 mM Spermidine, 2-5% NGSerum) and
884 incubated on ice for 10-15 minutes. then dounced 20 times with pestle A and another 20 times
885 with pestle B. Another 300 µL of NEB was added and the mixture was transferred to a 2mL tube
886 and incubated on a rotator at 4°C for 5 minutes, then filtered through a 70µm Flowmi strainer
887 (Sigma, Catalog #BAH136800070) into a fresh 2mL tube. The volume was adjusted to 1,200 µL
888 with more NEB if necessary and nuclei were lightly crosslinked by adding 6.52 µl of 37% FA,
889 incubating for 4 minutes at room temperature, and quenching with 133 µL 2.5 M Glycine solution.
890 Nuclei were finally isolated using density gradient separation, by adding 1,100 µL of O-
891 50% solution (generated by mixing 18,751 µL O-60%/OptiPrep/iodaxinol solution, 3242 µL H20,
892 450 µL NGS, and 22.5 µL 1M DTT) in a 5mL Eppendorf tube, then creating a density gradient by
893 adding 1,000 µL O-44% (8,800 µL O-50% plus 1,200 µL H_2O) to the very bottom of the tube and
894 500 µL O-22% (2,200 µL O-50% plus 2,800 NEB buffer) in between the O-44% and the top layer
895 with the nuclei. Tubes were then centrifuged for 30 minutes at 4°C with breaks off (deceleration
896 0, acceleration 5), and nuclei were extracted from the middle layer in the density gradient.
897 After nuclei isolation, nuclei were counted and approximately 100,000 were used as input
898 into each transposition reaction in four technical replicates for each individual mouse brain.
899 Transposition was carried out in 50 µL transposition mix, consisting of 25 µL 2x TD buffer (20 mM
900 Tris-HCl pH 7.6, 10 mM MgCl2, 20% Dimethyl Formamide), 22.5 µL nuclease-free H_2O, and 2.5
901 µL loaded Tn5 transposase (produced and assembled following previously established
902 protocols[136] by incubation in an Eppendorf ThermoMixer at 37°C at 1,000 rpm for 30 minutes. The
903 transposition reactions were then stopped immediately by adding 150 µL reverse crosslinking
904 buffer (1% SDS, 0.1M NaHCO3), and reverse crosslinking was carried out for 8 hours at 65°C.
905 Transposed DNA was isolated using the MinElute PCR Purification Kit (Qiagen, Catalog
906 #28004) by adding 600 µL PB Buffer and eluting in 20 µL EB Buffer heated to 65°C, then PCR
907 amplified by mixing 20 µL transposed DNA, 2.5 µL i5 and 2.5 µL i7 PCR primers, and 25 µL 2x
908 NEBNext High-Fidelity PCR Master Mix (New England Biolabs, Catalog #M0541L), with the
909 following settings: 72°C for 5 minutes, 98°C for 30 seconds, followed by 10 cycles of 98°C for 10
910 seconds, 63°C for 30 seconds, and 72°C for 45 seconds.
911 Final libraries were purified using the MinElute PCR Purification Kit (Qiagen, Catalog
912 #28004), QC-ed using a Qubit 1X dsDNA kit (Thermo Fisher Scientific, Catalog #Q33230) and an
913 Agilent TapeStation (High Sensitivity D1000 Screen Tape® Assay), and sequenced on a NextSeq
914 550 instrument in a 2x38 format.

915 ATAC-seq - data analysis

916 ATAC-seq data analysis was conducted largely as previously described[137], with brief specifics
917 provided below.
918 Two replicates were sequenced per brain sample, yielding *n*=16 total replicates from *n*=8
919 mice, of which *n*=4 were GDCA-exposed mice and *n*=4 were the corresponding vehicle control
920 mice (Supplementary Table 3).

Forward and reverse reads from each replicate were first trimmed to a length of 36bp using the script PEFastqToTabDelimited.py available at the following Github repository: https://github.com/georgimarinov/GeorgiScripts. Trimmed reads were aligned to both the entire mouse genome (mm10) and to the mitochondrial portion alone (chrM) using bowtie (v1.0.1). The following parameters were used for alignment to the mitochondrial genome: -p 20 -v 2 -a -t --best --strata -q -X 1000 --sam --12. The following parameters were used for alignment to the entire genome: -p 20 -v 2 -k 2 -m 1 -t --best --strata -q -X 1000 --sam --12.

The mitochondrial alignments were used to calculate the fraction of mitochondrial reads in each replicate (reported in Supplementary Table 3). For all subsequent analyses, the entire-genome alignments were used, after filtering out reads mapping to chrM.

The remaining, non-mitochondrial reads were deduplicated using the MarkDuplicates tool from Picard Tools (v1.99) using the following parameters: VALIDATION_STRINGENCY=LENIENT ASSUME_SORTED=true REMOVE_DUPLICATES=true. The resulting deduplicated .bam files were indexed using samtools v0.1.18 and converted to .wig using the script makewigglefromBAM-NH.py from the Github repository linked above. Reads per million (RPM) was used as the normalization method. The .wig files were converted to .bigWig using wigToBigWig from UCSC Utils (version from 2017-07-13). TSS enrichment scores reported in Supplementary Table 3 were calculated using the scripts signalAroundCoordinate-BW.py and ATACTSSscore.py, from the Github repository linked above. TSS coordinates were based on the UCSC mm10 refFlat gene annotation table (dated 2014-10-26).

Peaks were called for each replicate using the callpeak function from MACS2 (v2.1.1) using the following parameters: -g mm -f BAMPE --to-large -p 1e-1 --keep-dup all --nomodel. Then, reproducible peaks between replicates were identified using the previously described irreproducible discovery rate (IDR) framework[137]. IDR v2.0.4.2 was used for this step. The required script BAMPseudoReps.py from the Github repository linked above was converted to Python 3 using the 2to3 Python program prior to use.

The reproducible peaks between replicates per sample were then merged across samples using the createIterativeOverlapPeakSet.R script available at the following Github repository - https://github.com/corceslab/ATAC_IterativeOverlapPeakMerging - described in Grandi *et al.*, *Nature Protocols* 2022[138]. Blacklist regions provided to the script were downloaded from https://github.com/Boyle-Lab/Blacklist/tree/master/lists (file mm10-blacklist.v2.bed.gz) on July 11, 2025. The spm was set to 0 because confident peaks had already been identified. Additional relevant parameters were: --suffix _summits.bed --blacklist mm10-blacklist.v2.bed --genome mm10 --rule "(n+1)/2" --extend 250. This step yielded a .bed file with the coordinates of the final set of merged peaks, which was converted to SAF format and used to create a read counts table (rows = merged peaks, columns = samples) using featureCounts (v2.0.6) as follows: featureCounts -p --countReadPairs -B -C -T 8 -F SAF -a All_samples_peaks.saf -o All_Samples.counts <Brain1.pooled_replicates.sorted.bam> <Brain2.pooled_replicates.sorted.bam> <Brain3.pooled_replicates.sorted.bam>…

Samples were retained for subsequent analysis if both replicates had TSS enrichment scores ≥ 10, the standard deemed as “acceptable” under ENCODE guidelines for mm10 (https://www.encodeproject.org/atac-seq/, last accessed July 28, 2025). As per Supplementary Table 3, 7 samples (*n*=4 from GDCA-exposed mice, and *n*=3 from control mice) passed this filter.

Differentially accessible peaks were determined using DESeq2 (v1.42.1) using the default significance cutoff of alpha=0.10. These peaks were further annotated using the annotatePeaks.pl script from HOMER, which was installed using the configureHomer.pl script downloaded from http://homer.ucsd.edu/homer/ on July 14, 2025. Exact command used: annotatePeaks.pl sig_peak_file_for_homer.txt mm10 -annStats annotation_stats.txt > annotated_sig_peak_file.txt. The strand in sig_peak_file_for_homer.txt was specified as "." for all peaks.

Coverage of differentially accessible peaks (Fig. 5D; Fig. S10A-B) was determined as follows. First, BAM files for individual brains within each condition were merged using samtools v1.21. The resulting two files (one for control brains and one for GDCA-exposed brains) were sorted and indexed with samtools v1.21, and subsequently converted to bigWig format using the bamCoverage function from deepTools v3.3.0, using a bin size of 100 bp and specifying counts per million (CPM) as the normalization method. Coverage matrices per condition were generated from each bigWig file using the signalAroundCoordinate-individual.py script available from https://github.com/georgimarinov/GeorgiScripts, using the previously specified parameters[137], after conversion to Python 3 using the 2to3 Python program.

chromVAR[96] analysis (Figs. 5F and S11) was conducted using chromVAR 1.24.0, referencing the 0.99.6 version of the JASPAR 2024 database in R version 4.3.2.

Behavioral testing and measurement of core body temperature

Behavioral testing was conducted at the Stanford Behavioral and Functional Neuroscience Laboratory. Mice were acclimated to a reverse 12h-12h light-dark cycle for one week prior to initiation of experiments, ensuring that daytime testing coincided with their naturally active (dark) phase.

For experiments with mouse cohort 1 (schematized in Fig. 6A), mice were dosed for three consecutive days with GDCA (0.4 mg/kg) or saline vehicle (n=15 mice per group, n=30 total). Intravenous retroorbital injection was used as the administration route, with isoflurane as the anesthetic. The total injection volume was 50μL. Behavioral testing was conducted after the final injection (activity chamber: one day after final injection, Y-maze: two days after final injection). Mice were observed for one hour in the activity chamber and for five minutes in the Y-maze.

For experiments with mouse cohort 2 (schematized in Fig. 6B), mice were administered 50 mg/kg GDCA, 10 mg/kg GDCA, or saline vehicle *per os* (n=15 mice per group, n=45 total). Y-maze testing was conducted one hour post-dosing. Six days after Y-maze testing, all mice were redosed (keeping the same group assignments), and core body temperature was measured using a mouse rectal probe. All n=15 mice per group were measured at timepoint 0, prior to dosing; n=5 mice per group were measured at each subsequent timepoint (10min, 30min, and 60min post-dosing).

Data availability

All raw sequencing data are available under NCBI BioProject ID PRJNA1328687[139].

Code availability

All software, parameters, and relevant details of custom code are described in the Methods section.

Acknowledgements

We thank Jeff Rubin, Ren Song, Ayan Mondal, Hongchao Guo, Michael Bassik, Betsy Mellins, and Mark Kay for guidance surrounding brain endothelial cell culture and experiments. Jeff Rubin and Mark Kay provided us with the hCMEC/D3 cell line. We thank Jakub Rajnuk for advice during the metabolite selection process, Anshul Kundaje for guidance on RNA-seq data analysis, Garrett Patrick for reviewing the manuscript during its preparation, Ariel Gulasch for assistance with *in vitro* transcriptomic screening, and Rudy Wycallis at the Stanford Shared FACS Facility for assistance with flow cytometry. Several non-data figures such as experiment timeline figures were created using BioRender.com. This work was funded, in part, by NIH R01AI148623 and R01AI143757, NCI R01 CA301727, a Stand Up 2 Cancer Grant, and the Stanford Wu Tsai Neurosciences Institute. M.C. was supported by the National Defense Science and Engineering Graduate Fellowship. I.E.P. was supported by the Stanford REACH PhD fellowship. S.M.S. was supported by a Stanford Bio-X Bowes Fellowship. Computing costs were supported, in part, by an NIH S10 Shared Instrumentation grant (1S10OD02014101). The Stanford Behavioral and Functional Neuroscience Laboratory is supported by the NIH S10 Shared Instrumentation for Animal Research (1S10OD030452-01).

Author contributions

MC: conceptualization, investigation, methodology, data curation, formal analysis, visualization, writing - original draft, writing - review and editing. **SMS:** investigation, methodology. **IEP:** methodology. **DJR:** investigation, methodology. **GKM:** investigation, methodology, data curation, formal analysis. **AAM:** investigation, writing - review and editing. **JLEB:** investigation, methodology. **AN:** visualization. **JWJ:** methodology. **JCW:** supervision. **SXL:** methodology, supervision. **SMD:** methodology, supervision. **WJG:** supervision. **NLS:** investigation, methodology, data curation, formal analysis. **MS:** methodology, supervision. **AB:** funding acquisition, supervision. **TWC:** supervision. **ASB:** conceptualization, methodology, funding acquisition, supervision, writing - original draft, writing - review and editing. All authors read and approved the manuscript.

Competing interests

The authors declare no competing interests.

Supplementary information

Supplementary Information is available for this paper, as follows:

1. PDF of Supplementary Figures
2. Supplementary Table 1 - Properties of the 30 metabolites in the final screening panel
3. Supplementary Table 2 - Enriched KEGG pathways for genes upregulated by LPS
4. Supplementary Table 3 - Sample information for omics assays
5. Supplementary Table 4 - DESeq2 results, screen batches 1 and 2
6. Supplementary Table 5 - DESeq2 results, screen batches 3 and 4
7. Supplementary Table 6 - Differential genes in AD or PD pathways for 12 metabolites
8. Supplementary Table 7 - DESeq2 results, mouse brain RNA-seq
9. Supplementary Table 8 - GSEA results, mouse brain RNA-seq
10. Supplementary Table 9 - Significant differential splicing events in TMAO brains
11. Supplementary Table 10 - Studies associating GDCA in blood with AD, PD, or CI
12. Supplementary Table 11 - ATAC-seq data analysis results
13. Supplementary Table 12 - Full stats for behavioral and temperature data

References

1. Sachdev, P. S. *et al.* Factors predicting reversion from mild cognitive impairment to normal cognitive functioning: a population-based study. *PLoS One* **8**, e59649 (2013).
2. Shimada, H., Doi, T., Lee, S. & Makizako, H. Reversible predictors of reversion from mild cognitive impairment to normal cognition: a 4-year longitudinal study. *Alzheimers Res Ther* **11**, 24 (2019).
3. Badal, V. D. *et al.* The Gut Microbiome, Aging, and Longevity: A Systematic Review. *Nutrients* **12**, (2020).
4. Pang, S. *et al.* Longevity of centenarians is reflected by the gut microbiome with youth-associated signatures. *Nat Aging* **3**, 436–449 (2023).
5. Boehme, M., Guzzetta, K. E., Wasén, C. & Cox, L. M. The gut microbiota is an emerging target for improving brain health during ageing. *Gut Microbiome (Camb)* **4**, (2023).
6. Cryan, J. F. *et al.* The Microbiota-Gut-Brain Axis. *Physiological Reviews* (2019) doi:10.1152/physrev.00018.2018.
7. Loh, J. S. *et al.* Microbiota–gut–brain axis and its therapeutic applications in neurodegenerative diseases. *Signal Transduction and Targeted Therapy* **9**, 1–53 (2024).
8. Parker, A. *et al.* Fecal microbiota transfer between young and aged mice reverses hallmarks of the aging gut, eye, and brain. *Microbiome* **10**, 1–25 (2022).
9. D'Amato, A. *et al.* Faecal microbiota transplant from aged donor mice affects spatial learning and memory via modulating hippocampal synaptic plasticity- and neurotransmission-related proteins in young recipients. *Microbiome* **8**, 1–19 (2020).
10. Boehme, M. *et al.* Microbiota from young mice counteracts selective age-associated behavioral deficits. *Nat Aging* **1**, 666–676 (2021).
11. Wikoff, W. R. *et al.* Metabolomics analysis reveals large effects of gut microflora on mammalian blood metabolites. *Proceedings of the National Academy of Sciences* **106**, 3698–3703 (2009).
12. Lai, Y. *et al.* High-coverage metabolomics uncovers microbiota-driven biochemical

1077 landscape of interorgan transport and gut-brain communication in mice. *Nat Commun* **12**,
1078 6000 (2021).
1079 13. Wang, Z. *et al.* Gut flora metabolism of phosphatidylcholine promotes cardiovascular
1080 disease. *Nature* **472**, 57–63 (2011).
1081 14. Saeedi Saravi, S. S. *et al.* Gut microbiota-dependent increase in phenylacetic acid induces
1082 endothelial cell senescence during aging. *Nat Aging* **5**, 1025–1045 (2025).
1083 15. Knox, E. G., Aburto, M. R., Clarke, G., Cryan, J. F. & O'Driscoll, C. M. The blood-brain
1084 barrier in aging and neurodegeneration. *Molecular Psychiatry* **27**, 2659–2673 (2022).
1085 16. Shi, S. M. *et al.* Glycocalyx dysregulation impairs blood–brain barrier in ageing and
1086 disease. *Nature* **639**, 985–994 (2025).
1087 17. Panyard, D. J., Yu, B. & Snyder, M. P. The metabolomics of human aging: Advances,
1088 challenges, and opportunities. *Sci Adv* **8**, eadd6155 (2022).
1089 18. Menni, C. *et al.* Metabolomic markers reveal novel pathways of ageing and early
1090 development in human populations. *Int J Epidemiol* **42**, 1111–1119 (2013).
1091 19. Dunn, W. B. *et al.* Molecular phenotyping of a UK population: defining the human serum
1092 metabolome. *Metabolomics* **11**, 9–26 (2015).
1093 20. Darst, B. F., Koscik, R. L., Hogan, K. J., Johnson, S. C. & Engelman, C. D. Longitudinal
1094 plasma metabolomics of aging and sex. *Aging (Albany NY)* **11**, 1262–1282 (2019).
1095 21. Chen, H. *et al.* Highly multiplexed bioactivity screening reveals human and microbiota
1096 metabolome-GPCRome interactions. *Cell* **186**, 3095–3110.e19 (2023).
1097 22. Dekkers, K. F. *et al.* An online atlas of human plasma metabolite signatures of gut
1098 microbiome composition. *Nat Commun* **13**, 5370 (2022).
1099 23. Bishai, J. D. & Palm, N. W. Small Molecule Metabolites at the Host-Microbiota Interface. *J*
1100 *Immunol* **207**, 1725–1733 (2021).
1101 24. MahmoudianDehkordi, S. *et al.* Altered bile acid profile associates with cognitive
1102 impairment in Alzheimer's disease-An emerging role for gut microbiome. *Alzheimers*
1103 *Dement* **15**, 76–92 (2019).
1104 25. Low, D. Y. *et al.* Diet-Related Metabolites Associated with Cognitive Decline Revealed by
1105 Untargeted Metabolomics in a Prospective Cohort. *Mol Nutr Food Res* **63**, e1900177
1106 (2019).
1107 26. Chen, S.-J. *et al.* Alteration of Gut Microbial Metabolites in the Systemic Circulation of
1108 Patients with Parkinson's Disease. *J Parkinsons Dis* **12**, 1219–1230 (2022).
1109 27. Kijpaisalratana, N. *et al.* White matter hyperintensity severity modifies gut metabolite
1110 association with cognitive outcomes. *J Prev Alzheimers Dis* **12**, 100086 (2025).
1111 28. Marksteiner, J., Blasko, I., Kemmler, G., Koal, T. & Humpel, C. Bile acid quantification of 20
1112 plasma metabolites identifies lithocholic acid as a putative biomarker in Alzheimer's
1113 disease. *Metabolomics* **14**, 1–10 (2017).
1114 29. Bröer, S. *et al.* Alanine metabolism, transport, and cycling in the brain. *Journal of*
1115 *neurochemistry* **102**, (2007).
1116 30. Wishart, D. S. *et al.* HMDB 5.0: the Human Metabolome Database for 2022. *Nucleic Acids*
1117 *Res* **50**, D622–D631 (2021).
1118 31. Weksler, B., Romero, I. A. & Couraud, P.-O. The hCMEC/D3 cell line as a model of the
1119 human blood brain barrier. *Fluids Barriers CNS* **10**, 16 (2013).
1120 32. Sato, N. *et al.* Porphyromonas gingivalis lipopolysaccharide induces interleukin-6 and c-c
1121 motif chemokine ligand 2 expression in cultured hCMEC/D3 human brain microvascular
1122 endothelial cells. *Gerodontology* **39**, 139–147 (2022).
1123 33. Wilson 3rd, D. M. *et al*. Hallmarks of neurodegenerative diseases. *Cell* **186**, 693–714
1124 (2023).
1125 34. Xie, H. *et al.* The Role of Gut Microbiota-Derived Trimethylamine N-Oxide in the
1126 Pathogenesis and Treatment of Mild Cognitive Impairment. *International Journal of*
1127 *Molecular Sciences* **26**, 1373 (2025).

35. Melo, H. M. *et al.* Palmitate Is Increased in the Cerebrospinal Fluid of Humans with Obesity and Induces Memory Impairment in Mice via Pro-inflammatory TNF-α. *Cell Rep* **30**, 2180–2194.e8 (2020).
36. Lin, C.-H., Lin, Y.-N., Lane, H.-Y. & Chen, C.-J. The identification of a potential plasma metabolite marker for Alzheimer's disease by LC-MS untargeted metabolomics. *J Chromatogr B Analyt Technol Biomed Life Sci* **1222**, 123686 (2023).
37. Kalecký, K., German, D. C., Montillo, A. A. & Bottiglieri, T. Targeted Metabolomic Analysis in Alzheimer's Disease Plasma and Brain Tissue in Non-Hispanic Whites. *Journal of Alzheimer's Disease* (2022).
38. Chen, S.-J. *et al.* The Gut Metabolite Trimethylamine N-oxide Is Associated With Parkinson's Disease Severity and Progression. *Movement Disorders* **35**, 2115–2116 (2020).
39. Xu, Z. *et al.* Plasma trimethylamine N-oxide, carnitine, choline, and betaine distinguish cognition impairment in Parkinson's disease. *Parkinsonism Relat Disord* **135**, 107844 (2025).
40. Jonsson, A. L. *et al.* Impact of Gut Microbiota and Diet on the Development of Atherosclerosis in Apoe−/− Mice. *Arteriosclerosis, Thrombosis, and Vascular Biology* **38**, 2318 (2018).
41. Wei, W. *et al.* Psychological stress-induced microbial metabolite indole-3-acetate disrupts intestinal cell lineage commitment. *Cell metabolism* **36**, (2024).
42. Sankowski, B. *et al.* Higher cerebrospinal fluid to plasma ratio of p-cresol sulfate and indoxyl sulfate in patients with Parkinson's disease. *Clin Chim Acta* **501**, 165–173 (2020).
43. Pilitsis, J. G. *et al.* Quantification of Free Fatty Acids in Human Cerebrospinal Fluid. *Neurochemical Research* **26**, 1265–1270 (2001).
44. Sarrias, M. J., Cabré, P., Martínez, E. & Artigas, F. Relationship between serotoninergic measures in blood and cerebrospinal fluid simultaneously obtained in humans. *J Neurochem* **54**, 783–786 (1990).
45. Harnisch, L.-O. *et al.* Quantification of Bile Acids in Cerebrospinal Fluid: Results of an Observational Trial. *Biomedicines* **11**, 2947 (2023).
46. Wang, J. *et al.* Peripheral serum metabolomic profiles inform central cognitive impairment. *Sci Rep* **10**, 14059 (2020).
47. Bento, A. P. *et al.* An open source chemical structure curation pipeline using RDKit. *J Cheminform* **12**, 51 (2020).
48. Djousse, L. *et al.* Serum Individual Nonesterified Fatty Acids and Risk of Heart Failure in Older Adults. *Cardiology* **146**, 351–358 (2021).
49. Cui, Y. *et al.* Gas chromatography-mass spectrometry analysis of the free fatty acids in serum obtained from patients with Alzheimer's disease. *Biomed Mater Eng* **26 Suppl 1**, S2165–77 (2015).
50. Dou, L. *et al.* The cardiovascular effect of the uremic solute indole-3 acetic acid. *J Am Soc Nephrol* **26**, 876–887 (2015).
51. Lin, Y.-T. *et al.* Indole-3 acetic acid increased risk of impaired cognitive function in patients receiving hemodialysis. *Neurotoxicology* **73**, 85–91 (2019).
52. Nho, K. *et al.* Altered bile acid profile in mild cognitive impairment and Alzheimer's disease: Relationship to neuroimaging and CSF biomarkers. *Alzheimers Dement* **15**, 232–244 (2019).
53. Bain, M. A., Faull, R., Fornasini, G., Milne, R. W. & Evans, A. M. Accumulation of trimethylamine and trimethylamine- N -oxide in end-stage renal disease patients undergoing haemodialysis. *Nephrol Dial Transplant* **21**, 1300–1304 (2006).
54. Suzuki, T., Heaney, L. M., Bhandari, S. S., Jones, D. J. L. & Ng, L. L. Trimethylamine N-oxide and prognosis in acute heart failure. *Heart* **102**, 841–848 (2016).
55. Stubbs, J. R. *et al.* Serum Trimethylamine-N-Oxide is Elevated in CKD and Correlates with

Coronary Atherosclerosis Burden. *J Am Soc Nephrol* **27**, 305–313 (2016).
56. U.S. Department of Health and Human Services, Food and Drug Administration, Center for Drug Evaluation and Research (CDER). Guidance for Industry: Estimating the Maximum Safe Starting Dose in Initial Clinical Trials for Therapeutics in Adult Healthy Volunteers. *fda.gov* https://www.fda.gov/media/72309/download (2005).
57. Nair, A. B. & Jacob, S. A simple practice guide for dose conversion between animals and human. *J Basic Clin Pharm* **7**, 27–31 (2016).
58. Hoyles, L. *et al.* Regulation of blood-brain barrier integrity by microbiome-associated methylamines and cognition by trimethylamine N-oxide. *Microbiome* **9**, 235 (2021).
59. De Miguel, Z. *et al.* Exercise plasma boosts memory and dampens brain inflammation via clusterin. *Nature* **600**, 494–499 (2021).
60. Pornnoppadol, G. *et al.* Bispecific antibody shuttles targeting CD98hc mediate efficient and long-lived brain delivery of IgGs. *Cell Chem Biol* **31**, 361–372.e8 (2024).
61. Yang, A. C. *et al.* Physiological blood-brain transport is impaired with age by a shift in transcytosis. *Nature* **583**, 425–430 (2020).
62. Reinecke, F., Smeitink, J. A. M. & van der Westhuizen, F. H. OXPHOS gene expression and control in mitochondrial disorders. *Biochim Biophys Acta* **1792**, 1113–1121 (2009).
63. Zhu, A., Ibrahim, J. G. & Love, M. I. Heavy-tailed prior distributions for sequence count data: removing the noise and preserving large differences. *Bioinformatics* **35**, 2084–2092 (2019).
64. Zuo, J. *et al.* Glycolysis Rate-Limiting Enzymes: Novel Potential Regulators of Rheumatoid Arthritis Pathogenesis. *Frontiers in Immunology* **12**, 779787 (2021).
65. Zhou, R., Tardivel, A., Thorens, B., Choi, I. & Tschopp, J. Thioredoxin-interacting protein links oxidative stress to inflammasome activation. *Nat Immunol* **11**, 136–140 (2010).
66. Spector, R. Trimethylamine N-oxide induces inflammation and endothelial dysfunction in human umbilical vein endothelial cells via activating ROS-TXNIP-NLRP3 inflammasome. *Biochemical and Biophysical Research Communications* **481**, 63–70 (2016).
67. Li, D. *et al.* Trimethylamine-N-oxide promotes brain aging and cognitive impairment in mice. *Aging Cell* **17**, e12768 (2018).
68. Ximerakis, M. *et al.* Single-cell transcriptomic profiling of the aging mouse brain. *Nat Neurosci* **22**, 1696–1708 (2019).
69. Del Gatto-Konczak, F. *et al.* The RNA-Binding Protein TIA-1 Is a Novel Mammalian Splicing Regulator Acting through Intron Sequences Adjacent to a 5′ Splice Site. *Molecular and Cellular Biology* 6287–6299 (2023).
70. Xu, S. *et al.* SRRM2 organizes splicing condensates to regulate alternative splicing. *Nucleic Acids Res* **50**, 8599–8614 (2022).
71. Tagawa, T. *et al.* A virus-induced circular RNA maintains latent infection of Kaposi's sarcoma herpesvirus. *Proceedings of the National Academy of Sciences* **120**, e2212864120 (2023).
72. Campagne, S. *et al.* Molecular basis of RNA-binding and autoregulation by the cancer-associated splicing factor RBM39. *Nature Communications* **14**, 1–18 (2023).
73. Tollervey, J. R. *et al.* Analysis of alternative splicing associated with aging and neurodegeneration in the human brain. *Genome Res* **21**, 1572–1582 (2011).
74. Wang, Y. *et al.* rMATS-turbo: an efficient and flexible computational tool for alternative splicing analysis of large-scale RNA-seq data. *Nat Protoc* **19**, 1083–1104 (2024).
75. Grosz, B. R. *et al.* A novel synonymous KMT2B variant in a patient with dystonia causes aberrant splicing. *Molecular Genetics & Genomic Medicine* **10**, e1923 (2022).
76. Zech, M. *et al*. Haploinsufficiency of KMT2B, Encoding the Lysine-Specific Histone Methyltransferase 2B, Results in Early-Onset Generalized Dystonia. *The American Journal of Human Genetics* **99**, 1377–1387 (2016).
77. Hu, Z.-Y., Xiao, L., Bode, A. M., Dong, Z. & Cao, Y. Glycolytic genes in cancer cells are

more than glucose metabolic regulators. *J Mol Med (Berl)* **92**, 837–845 (2014).
78. Fan, Z. *et al.* The vascular gene Apold1 is dispensable for normal development but controls angiogenesis under pathological conditions. *Angiogenesis* **26**, 385–407 (2023).
79. Kim, K.-H., Won, J. H., Cheng, N. & Lau, L. F. The matricellular protein CCN1 in tissue injury repair. *J Cell Commun Signal* **12**, 273–279 (2018).
80. Shi, H. *et al.* Kruppel-like factor 2 protects against ischemic stroke by regulating endothelial blood brain barrier function. *Am J Physiol Heart Circ Physiol* **304**, H796–805 (2013).
81. Hatipoglu, O. F. *et al.* ADAMTS1 is a unique hypoxic early response gene expressed by endothelial cells. *J Biol Chem* **284**, 16325–16333 (2009).
82. Seo, J. H. *et al.* AKAP12 Supports Blood-Brain Barrier Integrity against Ischemic Stroke. *Int J Mol Sci* **21**, (2020).
83. Katsuoka, F. *et al.* Genetic evidence that small maf proteins are essential for the activation of antioxidant response element-dependent genes. *Mol Cell Biol* **25**, 8044–8051 (2005).
84. Smith, H. W. & Marshall, C. J. Regulation of cell signalling by uPAR. *Nature Reviews Molecular Cell Biology* **11**, 23–36 (2010).
85. Foltyn, M. *et al.* The physiological mTOR complex 1 inhibitor DDIT4 mediates therapy resistance in glioblastoma. *Br J Cancer* **120**, 481–487 (2019).
86. Hai, T., Wolfgang, C. D., Marsee, D. K., Allen, A. E. & Sivaprasad, U. ATF3 and stress responses. *Gene Expr* **7**, 321–335 (1999).
87. Yuniati, L., Scheijen, B., van der Meer, L. T. & van Leeuwen, F. N. Tumor suppressors BTG1 and BTG2: Beyond growth control. *Journal of Cellular Physiology* **234**, 5379–5389 (2019).
88. Huang, T., Yin, J., Ren, S. 'e & Zhang, X. Protective effects of KLF4 on blood-brain barrier and oxidative stress after cerebral ischemia-reperfusion in rats through the Nrf2/Trx1 pathway. *Cytokine* **169**, 156288 (2023).
89. Sangwung, P. *et al.* KLF2 and KLF4 control endothelial identity and vascular integrity. *JCI Insight* **2**, e91700 (2017).
90. Sayed, N. *et al.* Clinical trial in a dish using iPSCs shows lovastatin improves endothelial dysfunction and cellular cross-talk in LMNA cardiomyopathy. *Sci Transl Med* **12**, (2020).
91. Xu, D. & Li, C. Gene 33/Mig6/ERRFI1, an Adapter Protein with Complex Functions in Cell Biology and Human Diseases. *Cells* **10**, 1574 (2021).
92. Fritz, G. & Kaina, B. Transcriptional activation of the small GTPase gene rhoB by genotoxic stress is regulated via a CCAAT element. *Nucleic Acids Res* **29**, 792–798 (2001).
93. Luca, F. *et al.* Adaptive Variation Regulates the Expression of the Human SGK1 Gene in Response to Stress. *PLOS Genetics* **5**, e1000489 (2009).
94. Meng, F. *et al.* Genomic editing of intronic enhancers unveils their role in fine-tuning tissue-specific gene expression in Arabidopsis thaliana. *Plant Cell* **33**, 1997–2014 (2021).
95. ENCODE Project Consortium *et al.* Expanded encyclopaedias of DNA elements in the human and mouse genomes. *Nature* **583**, 699–710 (2020).
96. Schep, A. N., Wu, B., Buenrostro, J. D. & Greenleaf, W. J. chromVAR: inferring transcription-factor-associated accessibility from single-cell epigenomic data. *Nat Methods* **14**, 975–978 (2017).
97. Rauluseviciute, I. *et al.* JASPAR 2024: 20th anniversary of the open-access database of transcription factor binding profiles. *Nucleic Acids Res* **52**, D174–D182 (2024).
98. Jin, W. *et al*. Microbiota-derived bile acids antagonize the host androgen receptor and drive anti-tumor immunity. *Cell* **188**, 2336–2353.e38 (2025).
99. Klemm, S. L., Shipony, Z. & Greenleaf, W. J. Chromatin accessibility and the regulatory epigenome. *Nature Reviews Genetics* **20**, 207–220 (2019).
100. Janowsky, J. S. The role of androgens in cognition and brain aging in men. *Neuroscience* **138**, 1015–1020 (2006).
101. Jardí, F. *et al.* Testosterone boosts physical activity in male mice via dopaminergic

pathways. *Sci Rep* **8**, 957 (2018).
102. Davey, R. A. *et al.* Androgen Action via the Androgen Receptor in Neurons Within the Brain Positively Regulates Muscle Mass in Male Mice. *Endocrinology* **158**, 3684–3695 (2017).
103. Gräff, J. & Tsai, L.-H. The potential of HDAC inhibitors as cognitive enhancers. *Annu Rev Pharmacol Toxicol* **53**, 311–330 (2013).
104. Slijepcevic, D. *et al.* Hepatic uptake of conjugated bile acids is mediated by both sodium taurocholate cotransporting polypeptide and organic anion transporting polypeptides and modulated by intestinal sensing of plasma bile acid levels in mice. *Hepatology* **66**, 1631–1643 (2017).
105. Zhao, S. *et al.* Post sleeve gastrectomy-enriched gut commensal Clostridia promotes secondary bile acid increase and weight loss. *Gut Microbes* **17**, 2462261 (2025).
106. Qi, X. *et al.* Gut microbiota–bile acid–interleukin-22 axis orchestrates polycystic ovary syndrome. *Nature Medicine* **25**, 1225–1233 (2019).
107. Meessen, E. C. E. *et al.* Glycodeoxycholic Acid Inhibits Primary Bile Acid Synthesis With Minor Effects on Glucose and Lipid Homeostasis in Humans. *J Clin Endocrinol Metab* **110**, 1468–1477 (2025).
108. Monteiro-Cardoso, V. F., Corlianò, M. & Singaraja, R. R. Bile Acids: A Communication Channel in the Gut-Brain Axis. *Neuromolecular Med* **23**, 99–117 (2021).
109. Yu, S. *et al.* Glutamatergic Preoptic Area Neurons That Express Leptin Receptors Drive Temperature-Dependent Body Weight Homeostasis. *J. Neurosci.* **36**, 5034–5046 (2016).
110. Uchino, E. *et al.* Identification of hypothermia-inducing neurons in the preoptic area and activation of them by isoflurane anesthesia and central injection of adenosine. *J Physiol Sci* **74**, 33 (2024).
111. Taylor, T. N., Greene, J. G. & Miller, G. W. Behavioral phenotyping of mouse models of Parkinson's disease. *Behavioural Brain Research* **211**, 1–10 (2010).
112. Yalçin, M., Grande, V., Outeiro, T. F. & Relógio, A. Circadian clock dysfunction in Parkinson's disease: mechanisms, consequences, and therapeutic strategy. *NPJ Parkinsons Dis* **11**, 213 (2025).
113. Kirshenbaum, G. S., Dachtler, J., Roder, J. C. & Clapcote, S. J. Characterization of cognitive deficits in mice with an alternating hemiplegia-linked mutation. *Behav Neurosci* **129**, 822–831 (2015).
114. Heredia-López, F. J. *et al.* An automated Y-maze based on a reduced instruction set computer (RISC) microcontroller for the assessment of continuous spontaneous alternation in rats. *Behav Res Methods* **48**, 1631–1643 (2016).
115. Bendl, J. *et al.* The three-dimensional landscape of cortical chromatin accessibility in Alzheimer's disease. *Nat Neurosci* **25**, 1366–1378 (2022).
116. Li, X. *et al.* Transcriptional and epigenetic decoding of the microglial aging process. *Nature Aging* **3**, 1288–1311 (2023).
117. Canyelles, M. *et al.* Gut Microbiota-Derived TMAO: A Causal Factor Promoting Atherosclerotic Cardiovascular Disease? *Int J Mol Sci* **24**, (2023).
118. Stilling, R. M. *et al.* Social interaction-induced activation of RNA splicing in the amygdala of microbiome-deficient mice. *Elife* **7**, (2018).
119. Thion, M. S. *et al*. Microbiome Influences Prenatal and Adult Microglia in a Sex-Specific Manner. *Cell* **172**, 500–516.e16 (2018).
120. Kaur, H., Singh, Y., Singh, S. & Singh, R. B. Gut microbiome-mediated epigenetic regulation of brain disorder and application of machine learning for multi-omics data analysis. *Genome* **64**, 355–371 (2021).
121. Molinaro, A. *et al.* Imidazole propionate is increased in diabetes and associated with dietary patterns and altered microbial ecology. *Nat Commun* **11**, 5881 (2020).
122. Shah, S. N. *et al.* Cerebrovascular damage caused by the gut microbe/host co-metabolite p-cresol sulfate is prevented by blockade of the EGF receptor. *Gut Microbes* **16**, 2431651

(2024).
123. Ticinesi, A., Guerra, A., Nouvenne, A., Meschi, T. & Maggi, S. Disentangling the Complexity of Nutrition, Frailty and Gut Microbial Pathways during Aging: A Focus on Hippuric Acid. *Nutrients* **15**, (2023).
124. Li, M. *et al.* Gut microbiota metabolite indole-3-acetic acid maintains intestinal epithelial homeostasis through mucin sulfation. *Gut microbes* **16**, (2024).
125. Mayhan, W. G. VEGF increases permeability of the blood-brain barrier via a nitric oxide synthase/cGMP-dependent pathway. *Am J Physiol* **276**, C1148–53 (1999).
126. Qing, Y. *et al.* Targeted metabolomics reveals aberrant profiles of serum bile acids in patients with schizophrenia. *Schizophrenia (Heidelb)* **8**, 65 (2022).
127. Pavlova, T. *et al.* Urinary intermediates of tryptophan as indicators of the gut microbial metabolism. *Anal Chim Acta* **987**, 72–80 (2017).
128. Yang, B. *et al.* HIV-Differentiated Metabolite N-Acetyl-L-Alanine Dysregulates Human Natural Killer Cell Responses to Mycobacterium tuberculosis Infection. *International Journal of Molecular Sciences* **24**, 7267 (2023).
129. Green, M. R. & Sambrook, J. Precipitation of RNA with Ethanol. *Cold Spring Harb Protoc* **2020**, 101717 (2020).
130. Bray, N. L., Pimentel, H., Melsted, P. & Pachter, L. Near-optimal probabilistic RNA-seq quantification. *Nature Biotechnology* **34**, 525–527 (2016).
131. Love, M. I., Huber, W. & Anders, S. Moderated estimation of fold change and dispersion for RNA-seq data with DESeq2. *Genome Biol* **15**, 550 (2014).
132. Raudvere, U. *et al.* g:Profiler: a web server for functional enrichment analysis and conversions of gene lists (2019 update). *Nucleic Acids Res* **47**, W191–W198 (2019).
133. Garrido-Martín, D., Palumbo, E., Guigó, R. & Breschi, A. ggsashimi: Sashimi plot revised for browser- and annotation-independent splicing visualization. *PLoS Comput Biol* **14**, e1006360 (2018).
134. Liu, B. B. et al. Dissecting regulatory syntax in human development with scalable multiomics and deep learning. Preprint at https://www.biorxiv.org/content/10.1101/2025.04.30.651381v1 (2025).
135. Marinov, G. K., Shipony, Z., Kundaje, A. & Greenleaf, W. J. Genome-Wide Mapping of Active Regulatory Elements Using ATAC-seq. *Methods Mol Biol* **2611**, 3–19 (2023).
136. Picelli, S. *et al.* Tn5 transposase and tagmentation procedures for massively scaled sequencing projects. *Genome Res* **24**, 2033–2040 (2014).
137. Marinov, G. K. & Shipony, Z. Interrogating the Accessible Chromatin Landscape of Eukaryote Genomes Using ATAC-seq. *Methods Mol Biol* **2243**, 183–226 (2021).
138. Grandi, F. C., Modi, H., Kampman, L. & Corces, M. R. Chromatin accessibility profiling by ATAC-seq. *Nat Protoc* **17**, 1518–1552 (2022).
139. Systematic identification of age-related microbiome metabolites that impact the brain. National Center for Biotechnology Information. https://www.ncbi.nlm.nih.gov/bioproject/PRJNA1328687 (2025).